



HIE-ISOLDE HEBT beam optics studies with MADX

A. Parfenova, J. Bauche, M.A. Fraser, B. Goddard, M. Martino & D. Voulot

Abstract

Beam design and beam optics studies for the HIE-ISOLDE transfer lines [1, 2] have been carried out in MADX [3], and benchmarked against TRACE 3-D results [4, 5, 6]. Magnet field errors and alignment imperfections leading to deviations from design parameters have been treated explicitly, and the sensitivity of the machine lattice to different individual error sources was studied. Errors of different types have been considered and their effects on the machine have been corrected [7]. As a result, the tolerances for the various error contributions have been specified for the different equipment systems. The design choices for the expected magnet field and power supply quality, alignment tolerances, instrument resolution and physical apertures were validated.

The baseline layout contains three identical branch lines as presented in Fig. 1. The detailed beam optics study with MADX was carried out for the beam line XT01. The large energy range from 0.3 to 10 MeV/u requested for the experiments sets a number of challenging constraints on the beam optics design. The facility is optimized for energies 5.5 and 10 MeV/u. However, some experiments will be carried out at 0.3 MeV/u, where the beam emittance is rather large. Thus the beam transmission at the low energy of 0.3 MeV/u was studied in detail. The dependence of the beam transmission on the geometric beam emittance was investigated. Beam sizes at the target for different energies were estimated and compared with the design values for experiments. All simulations were done for a mass-charge ratio $A/q=4.5$, representing the most demanding beams for field specification.

The methodology and results of the studies are presented. The study details and complementary material are documented in Appendix. MADX beam optics simulations are found on DFS [9].

Geneva, Switzerland

October 2013



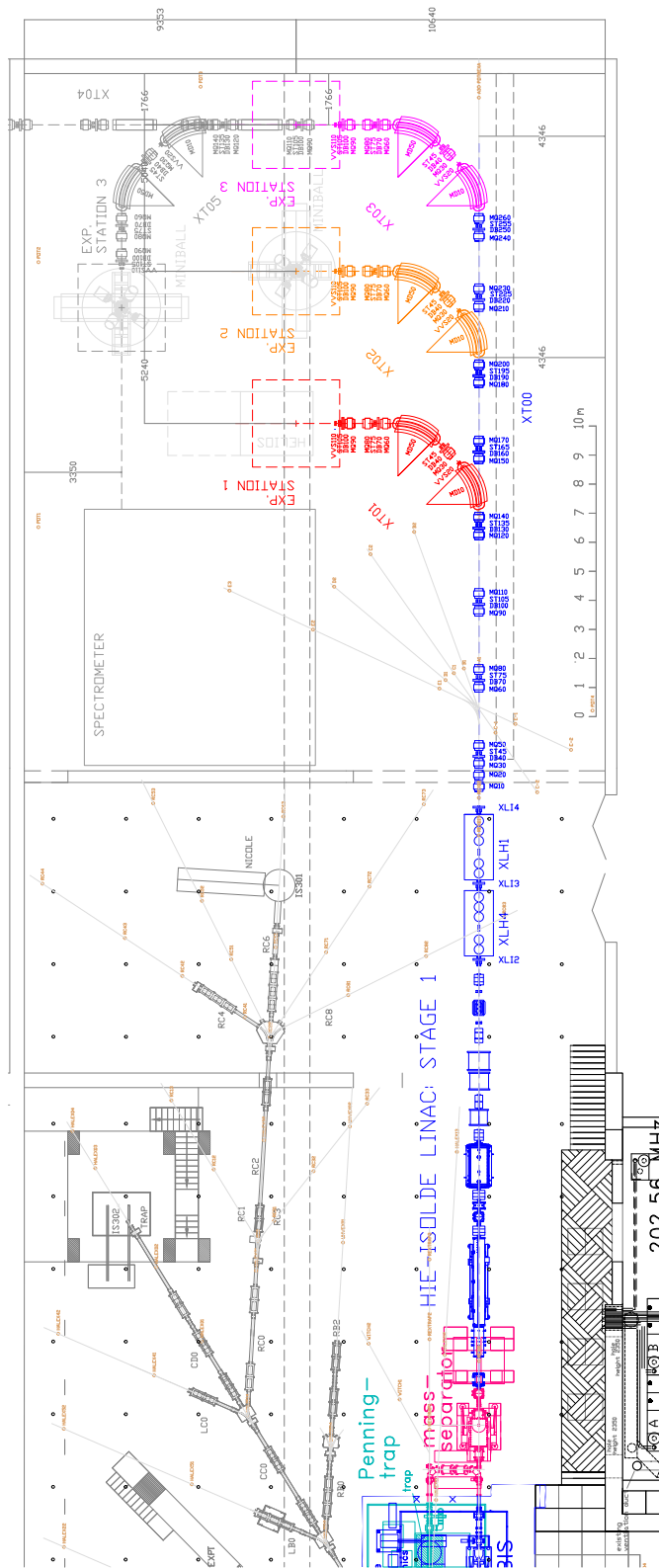


Figure 1: HIE-ISOLDE beam line layout.

Contents

1	Purpose of Error-Study	4
2	Error classification and excepted tolerances	4
3	XT01 modeling	4
3.1	Trajectory correction algorithms	4
3.1.1	Global	5
3.1.2	Piecewise	5
3.2	Correction of static errors (10 MeV/u)	5
3.2.1	Steerer specification	6
3.2.2	Orthogonal steering	9
3.3	Dynamic errors	11
3.4	Beam sizes at the target	12
3.5	Beam transmission at 0.3 MeV/u	13
3.5.1	Particle tracking vs. twiss	13
3.5.2	Accuracy of the linear optics approximation	14
3.5.3	Beam transmission for many error seeds	14
3.6	Bunch length estimates at the experiments	17
4	Conclusion and Outlook	18
5	Acknowledgement	19
6	References	19
7	APPENDIX	20
7.1	Individual static error sources	20
7.1.1	Dipole errors	20
7.1.2	Quadrupole errors	20
7.1.3	Initial conditions	20
7.1.4	Malfunction of beam position monitors	21
7.1.5	Remnant field considerations	22
7.2	TRACE3D to MADX conversion: major aspects	22
7.2.1	Steffen's matrix	23
7.2.2	Ptc_track syntax	23
7.2.3	Orthogonal steering MADX syntax	24
7.3	Reduction of steerers and monitors	25
7.4	Estimate of beam transmission via remaining acceptance	27
7.5	Particle distributions: 0.3, 5.9 and 10 MeV/u ($A/q=4.5$)	28
7.6	Beam transmission at 0.3 MeV/u: benchmarking of ptc_track collimation	30
7.7	Magnets' nonlinear components	30
7.7.1	Integrated multipoles in MADX conversion	32
7.7.2	Sextupolar and octupolar components in dipoles	32
7.7.3	Steerers misalignment and sextupolar components. Multipoles in quadrupoles	32
7.7.4	Harmonic components for HIE-ISOLDE new magnets	34

1 Purpose of Error-Study

Magnet field errors and alignment imperfection introduce trajectory distortions, detuning and betatron coupling errors, which affect β - and dispersion functions, all together leading to deviation from set design parameters [7]. Sensitivity of the machine’s lattice to different error sources needs to be investigated and implies requirements on tolerances and correction algorithms. Contributions from different error sources were estimated quantitatively in order to validate the following design choices:

power supply ripple, alignment tolerances, magnet field quality, instrument resolution, physical apertures and steering power.

2 Error classification and excepted tolerances

Different possible error sources of static and dynamic nature were considered. The impact of each error source was evaluated using MADX simulation; their tolerances are listed in Table 1. The error in the beam position and divergence on entering the HEBT are summarized by the initial conditions [5]. Dipole and quadrupole power ripple $\Delta I/I$ are the main sources of dynamic errors; their accepted tolerances are given in Sec. 3.3.

Table 1: Accepted tolerances for static error sources.

Error source	Value	Distribution
Dipole field, $\Delta B_{dl}/B_{dl}$	$1.0 \cdot 10^{-3}$	uniform
roll angle $d\psi$, rad	$2.0 \cdot 10^{-4}$	uniform
longitudinal position dS , m	$1.0 \cdot 10^{-3}$	uniform
Quadrupole field, $\Delta K/K$	$1.0 \cdot 10^{-3}$	uniform
shift dX , dY , m	$2.5 \cdot 10^{-4}$	Gauss(σ)
Initial conditions dX , dY , m	$5.0 \cdot 10^{-4}$	Gauss(σ)
dpx , dpy , mrad	$5.0 \cdot 10^{-4}$	Gauss(σ)
Monitor shift dX , dY , m	$2.5 \cdot 10^{-4}$	Gauss(σ)
resolution X , Y , m	$2.0 \cdot 10^{-4}$	uniform

3 XT01 modeling

Nominal optics for XT01 calculated in MADX is shown in Fig. 2. Individual random errors (Table 1) were introduced in the MADX simulation via following steps:

(1) including errors, (2) generating optics and trajectory, (3) correcting trajectory, (4) recalculating optics and corrected trajectory.

Details of the simulation for each error source and the corresponding MADX syntax are given in Sec. 7.1 [3].

3.1 Trajectory correction algorithms

Trajectory correction is essential to minimize beam loss. Trajectory distortion from residual misalignment and field errors (static errors) was corrected by the two methods: global and piecewise. Note, that an additional beam monitor at the target was considered in the correction algorithms.

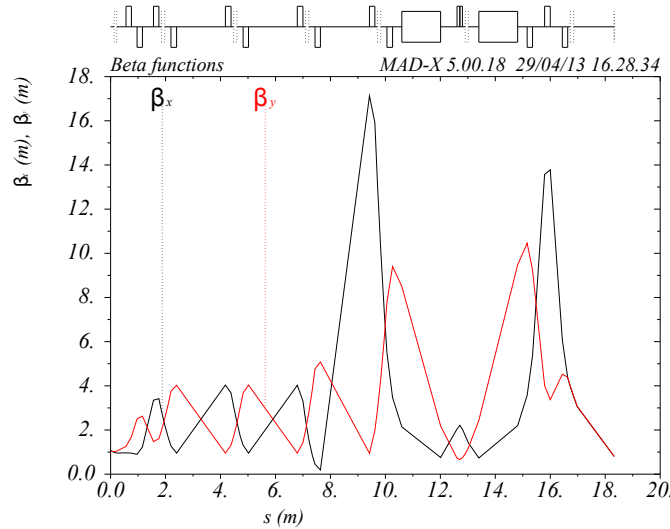


Figure 2: Nominal optics for XT01 beam line: β -functions.

3.1.1 Global

Global correction is performed by built in MADX micado correction algorithm [3]. It takes all monitors and correctors present in the beam line and minimizes the trajectory distortion at all monitors.

3.1.2 Piecewise

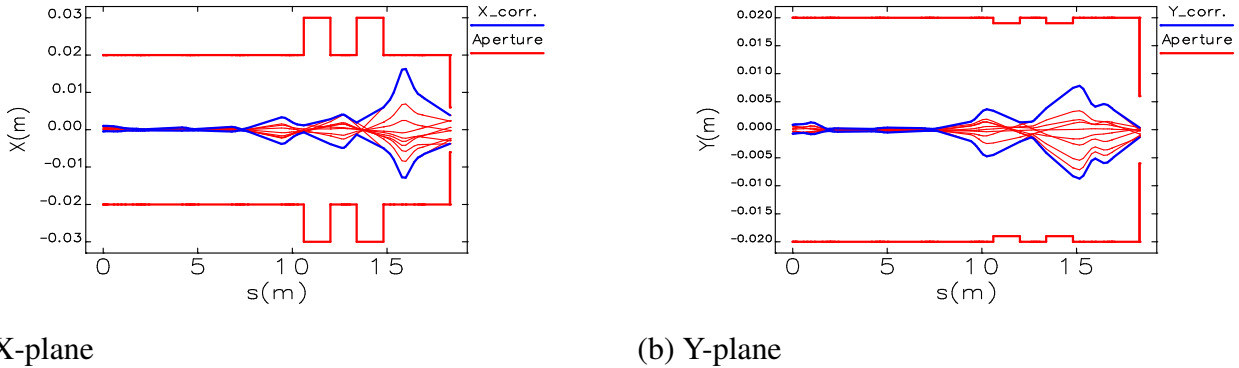


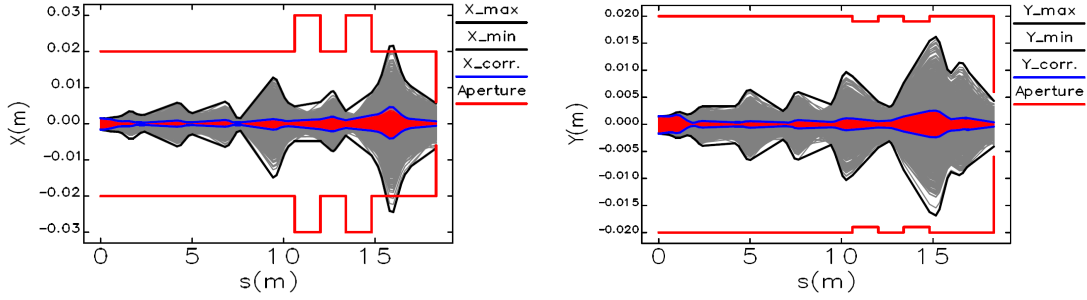
Figure 3: Piecewise trajectory correction performed for the part of the beam line by using only the first three steerers in XT01.

The piecewise correction is a combination of segment-by-segment corrections done over a short range consecutively alternating steerers one by one and correcting the trajectory at the next monitor downstream of the steerer. An example of the piecewise correction in X-/Y- planes using only the first three steerers out of six available in XT01 (10 seeds simulation) is shown in Fig. 3 demonstrates.

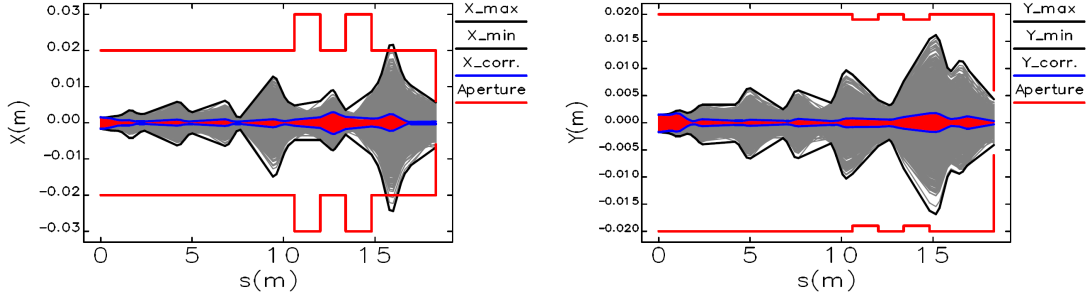
3.2 Correction of static errors (10 MeV/u)

X-/Y- trajectories, dispersion and β -functions before/after the trajectory correction of *all static errors* in 1000 seeds simulation are shown in Fig. 4 and 5 *. Red solid line represents the beamline aperture.

*Data plots for most pictures were done using SDDS-toolkit [8].

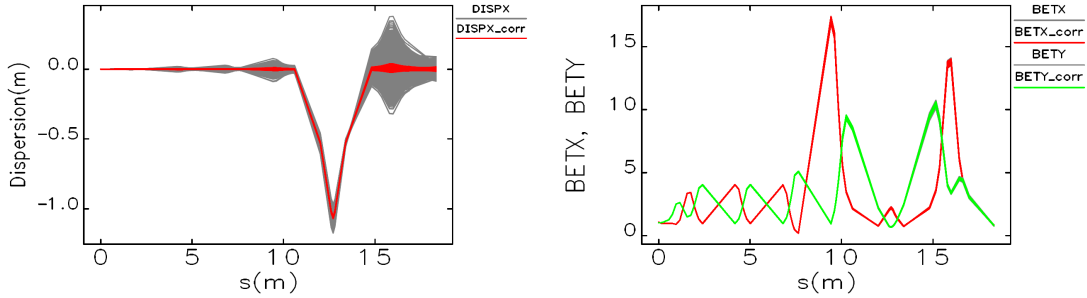


(top) Global correction in X-/Y-



(bottom) Piecewise correction in X-/Y-

Figure 4: *Global* (top) and *piecewise* (bottom) trajectory correction of *all static errors* in X-/Y- planes, respectively.



(a) Dispersion function

(b) β -functions

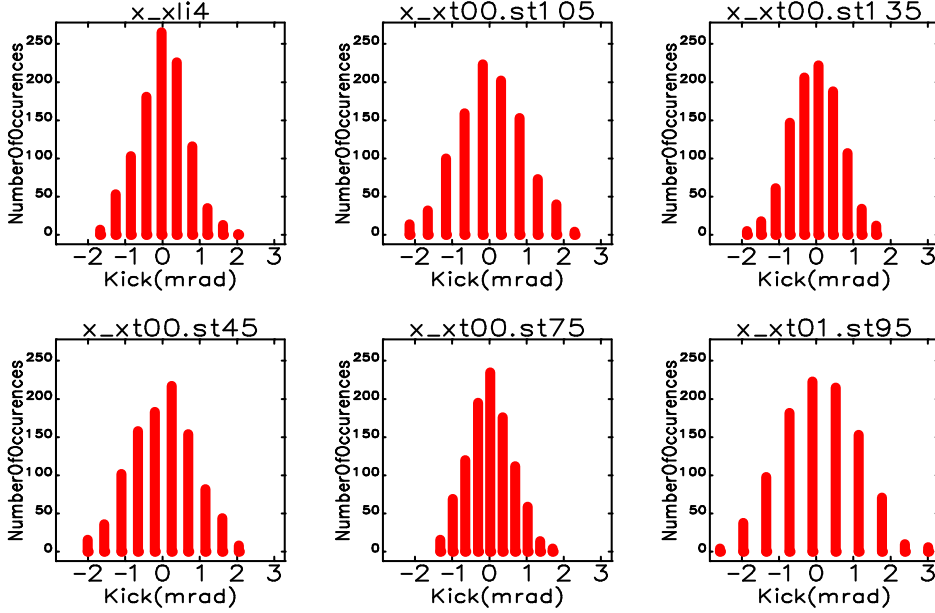
Figure 5: Dispersion and β -functions before and after *global* trajectory correction of *all static errors*.

3.2.1 Steerer specification

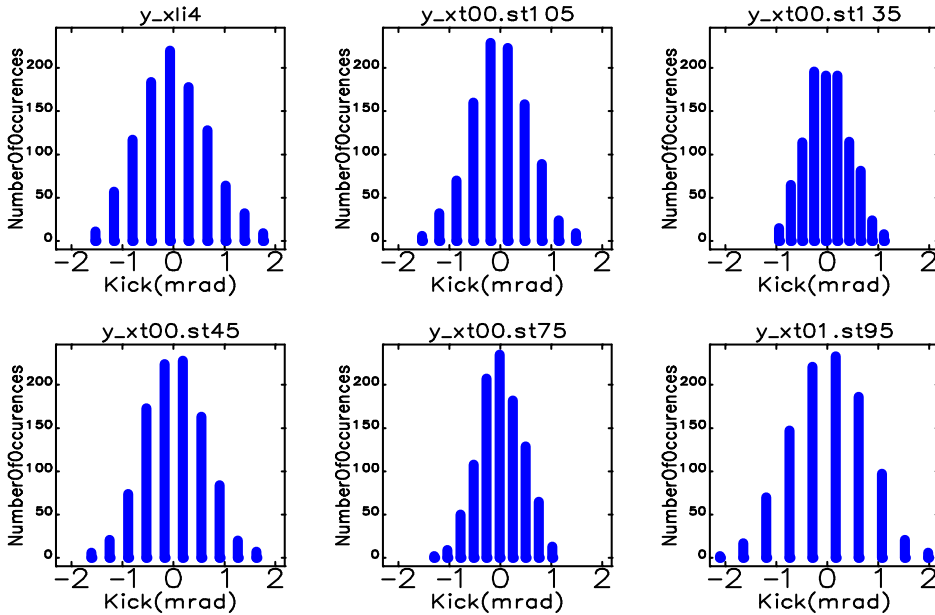
Steerer strengths (Figs. 6 and 7) used in the correction of *all static errors* (Fig. 4) are less than ± 2 mrad (for both correction algorithms), which are within the foreseen steering power (Table 2). *The maximum deflection angles* $\theta_{corr.max}$ at different energies are calculated with ± 6 Tmm, which correspond to ± 48 A. An average steering power required for the trajectory correction of all static errors can be estimated as *one sigma* of a Gaussian distribution (68%) and is less than approximately 1 mrad [10].

Table 2: Beam energies and maximum deflection angles.

	0.3 MeV/u	5.9 MeV/u	10 MeV/u
$B\rho, Tm$	0.355	1.575	2.054
$\theta_{corr. max}, mrad$	16.92	3.81	2.92

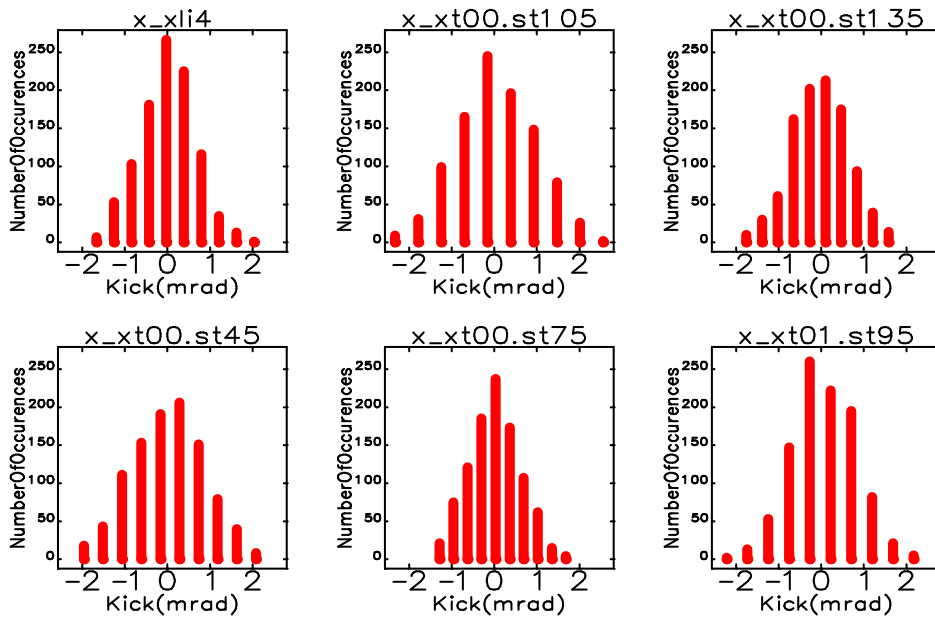


(top) X- steerers

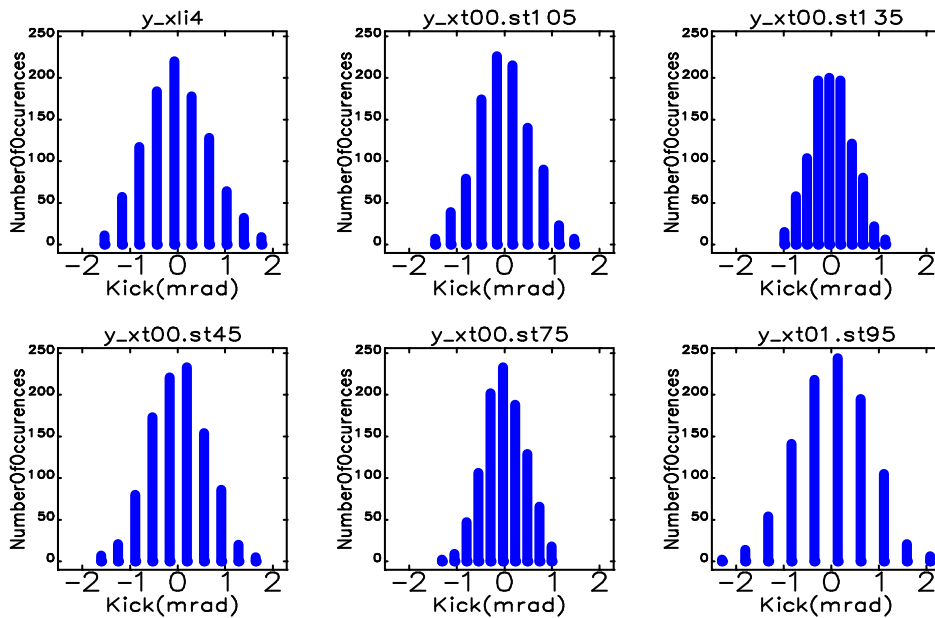


(bottom) Y- steerers

Figure 6: X- (top) /Y- (bottom) steerer strengths used in the *global* trajectory correction (1000 seeds).



(top) X- steerers



(bottom) Y- steerers

Figure 7: X- (top) /Y- (bottom) steerer strengths used in the *piecwise* trajectory correction (1000 seeds).

3.2.2 Orthogonal steering

If the experimental set-up is not perfectly aligned it is important to have sufficient steering power to bring the beam on axis at the target. The orthogonal steering is a complementary correction used for the final correction of the beam centroid and angle at the target applied on top of the trajectory correction of residual field and misalignment errors.

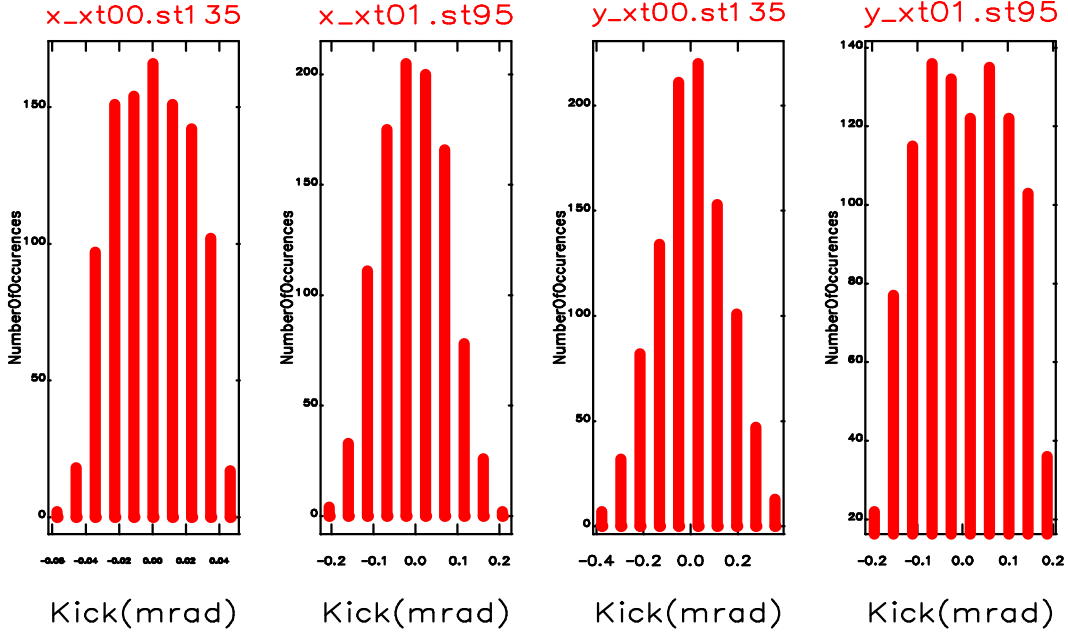


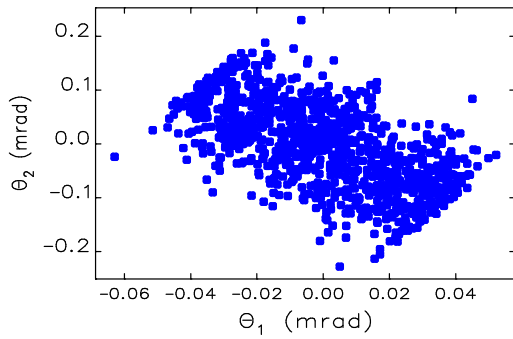
Figure 8: Orthogonal steering: complementary steerer strengths.

After the trajectory correction of the beam centroid there still exists a finite divergence in (x, x', y, y') at the target, which can be corrected to zero ($x = y = x' = y' = 0$) by a unique setting of two correction angles of the two last steerers before the target. The complementary correction angles found in 1000 seeds simulation (Fig. 8) for the two steerers (XT00.ST135 and XT01.ST95) are within ± 0.4 mrad, which is about 5-10% of their maximum deflection angles equal to 2.92 mrad at 10 MeV/u (see also Sec. 3.2.1). The 2D plot of the found settings is shown in Fig. 9, MADX syntax details for orthogonal steering are given in Sec. 7.2.3. Note that XT01.ST105 was renamed into XT01.ST95 for the layout version 6 (see monitor and steerer reduction in Sec. 7.3.).

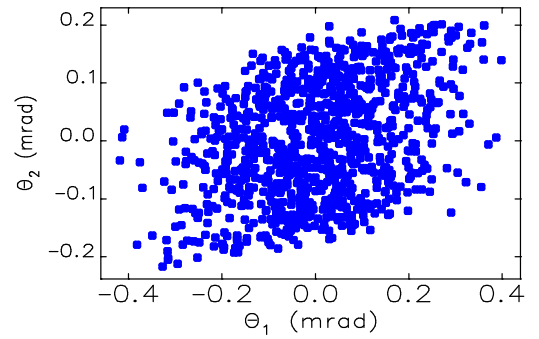
The maximum possible correction angles of the two steerers (θ_1 and θ_2) without intersecting with the beam aperture and exceeding their maximum deflection angles put limits on the acceptable error in position and tilt of the target axis. The maximum correction angles are specified by the beam envelope of two sigma starting to hit the aperture (Fig. 10), where the *one sigma* beam size is defined by

$$\sigma_x = \sqrt{\epsilon_x \cdot \beta_x + (\sigma_{\Delta p/p} \cdot D_x)^2}, \quad \sigma_y = \sqrt{\epsilon_y \cdot \beta_y}. \quad (1)$$

Available phase-space areas in (x, x') and (y, y') of the corresponding target misalignment are shown in Fig. 11.

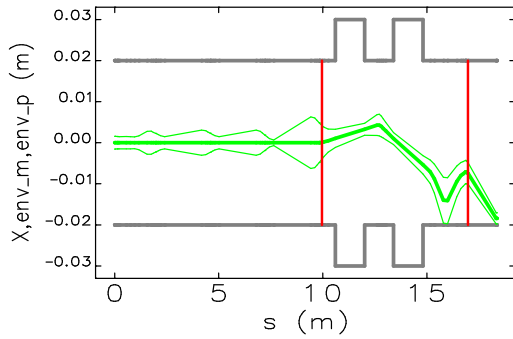


(a) X- plane

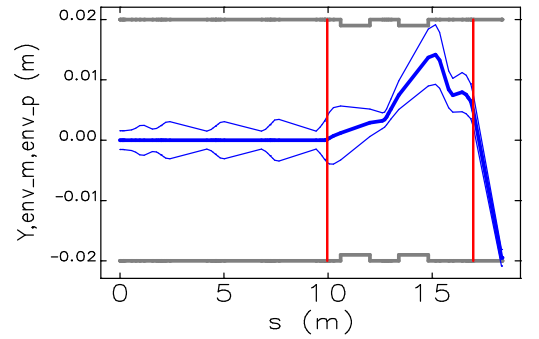


(b) Y- plane

Figure 9: Orthogonal steering: an alternative representation of the complementary steerer strengths for XT00.ST135 (θ_1) and XT01.ST95 (θ_2).

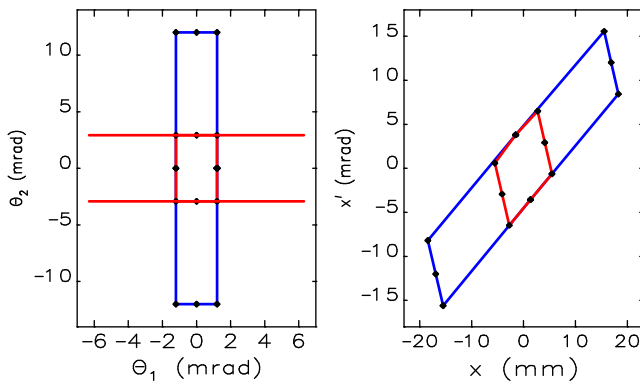


(a) X- plane

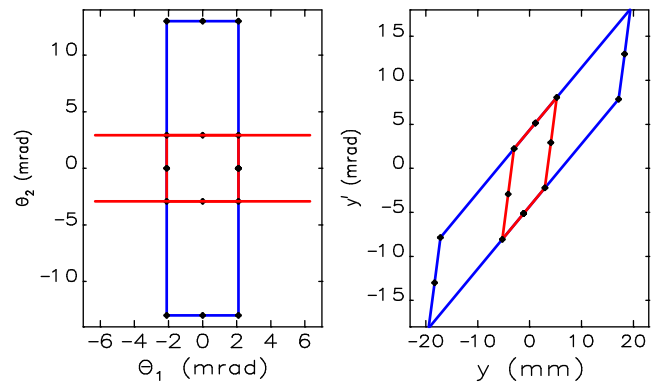


(b) Y- plane

Figure 10: *Two sigma* beam envelope hitting the aperture. Red vertical lines indicate steerer positions.



(a) X- plane



(b) Y- plane

Figure 11: The limits at the target are defined by the physical aperture (blue line) and by the maximum deflection angles of the steerers at 10 MeV/u (red line).

3.3 Dynamic errors

The design energies for HIE-ISOLDE are 5.5 and 10 MeV/u for $A/q < 4.5$ as specified in the physics case for the project and limitations of the normal conducting linac that will remain even after the upgrade. However, beams of lower A/q and energies can also be accelerated. The beam rigidity will range from 0.158 Tm (0.3 MeV/u, $A/q = 2$) to 2.054 Tm (10 MeV/u, $A/q = 4.5$). The quadrupole gradient will vary by a factor of about three between the strongest and weakest focussing quadrupole in the HEBT (the strongest gradient being found in the matching section at the linac output). Therefore, the current in the quadrupoles in the HEBT will typically range from 2 A to 100 A.

Dipole and quadrupole power ripple are main sources of dynamic errors; their tolerances for 0.3 (low), 5.9 (middle) and 10 (top) MeV/u energies are summarized in Table 3. Trajectory distortion caused by the power ripple is rather small (tiny) at the middle/top energies and is quite large (significant) at the low energy (Figs. 12 and 13). Note that trajectory distortion caused by *dynamic errors* can't be corrected. Thus, at 0.3 MeV/u dynamic errors introduce a dilution to the X-beam spot at the target with a sigma of 0.3 mm (Fig. 14). *Trajectory envelopes* at the low energy are shown in Fig. 15.

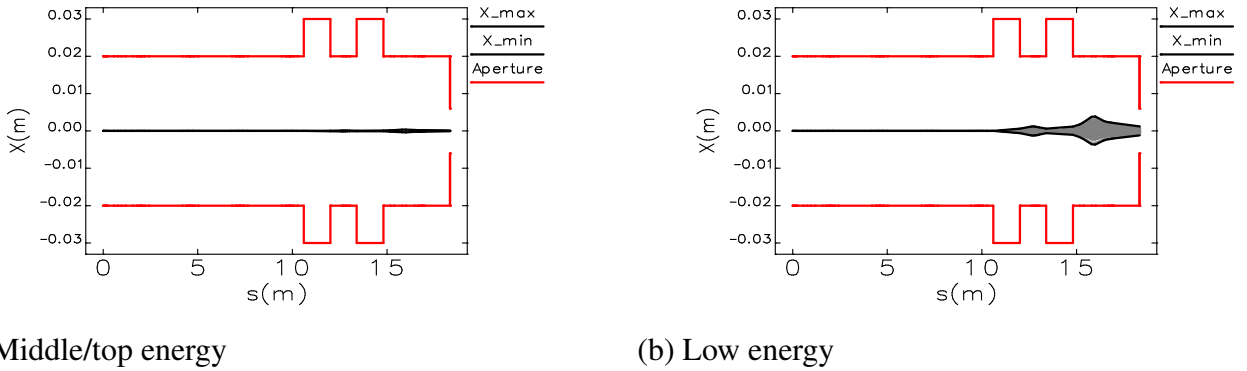


Figure 12: Trajectory distortion due to dipole power ripple (Table 3).

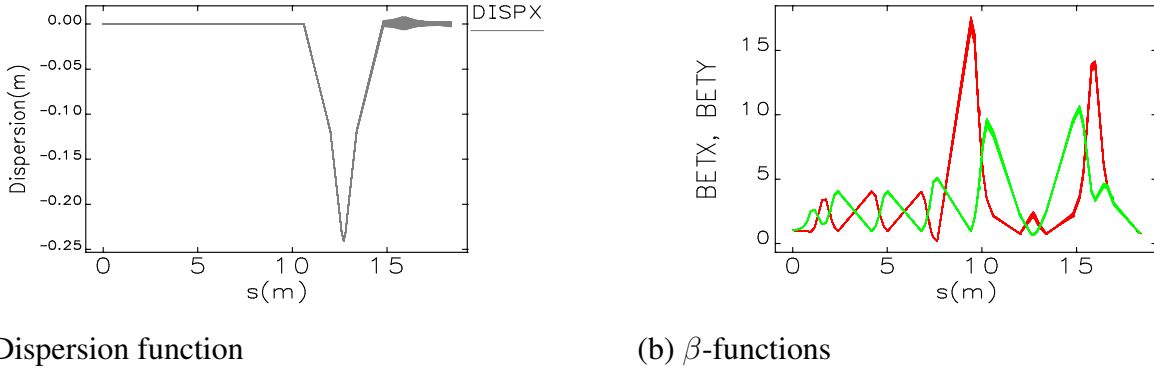


Figure 13: Distortion of the dispersion and β -functions due power ripple at the low energy (0.3 MeV/u).

Table 3: Dynamic errors: accepted tolerances for $\Delta I/I$.

energy	middle/top	low	Distribution
Dipoles	$\pm 1.18 \cdot 10^{-4}$	$\pm 1.18 \cdot 10^{-3}$	uniform
Quadrupoles	$\pm 1.4 \cdot 10^{-4}$	$\pm 1.4 \cdot 10^{-3}$ (some $\pm 1.0 \cdot 10^{-2}$)	uniform

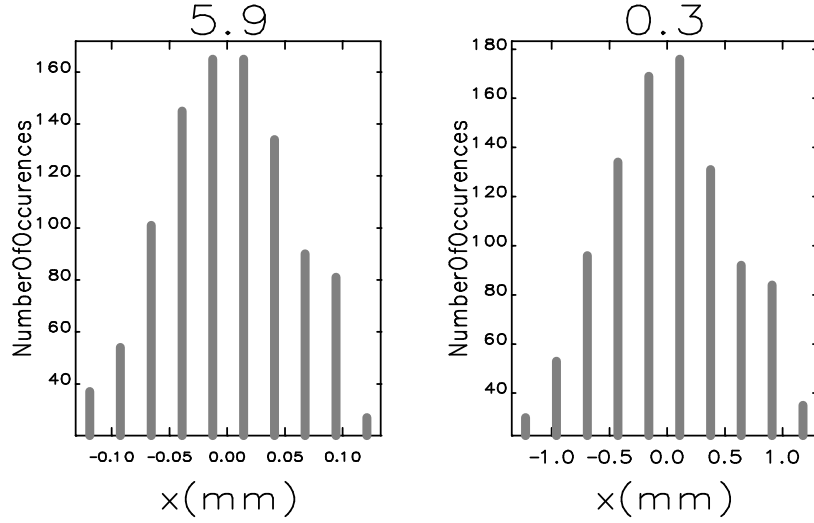


Figure 14: X-distributions at the target (dilution of X-beam spot) caused by dynamic errors: $\sigma = 0.03$ mm at middle/top and $\sigma = 0.3$ mm at low energy.

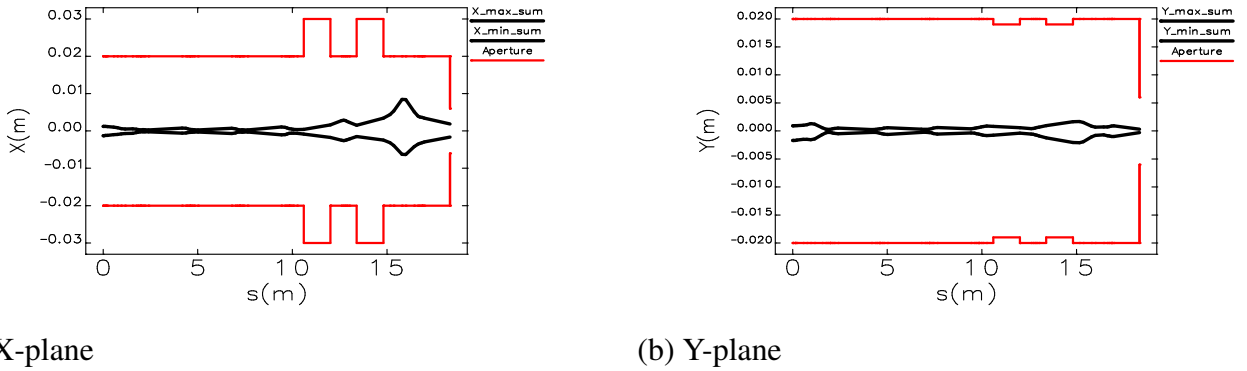


Figure 15: Trajectory envelopes after the global correction of *all static errors* (Fig. 4) and trajectory distortion due to dynamic errors at 0.3 MeV/u on top [Fig. 12 (b)].

3.4 Beam sizes at the target

Experiments request 3-4 mm X-/Y- beam spots at the target for all energies.

The *beam spot* is defined to be equal to $\pm 2\sigma_{x/y}$ in Eq. (1), where the beam emittances ϵ_x , ϵ_y and $\sigma_{\Delta p/p}$ are taken from Table 4 in Sec. 7.5, and β -functions at the target are $\beta_x = \beta_y = 0.81$ m. Simulations for 1000 seeds are presented in Fig. 16: estimated average X-/Y- beam spots at the target are about 2.7 mm at 10 MeV/u; 3 mm at 5.9 MeV/u and 6 mm at 0.3 MeV/u with the dilution of 0.3 mm from the power ripple of dipole and quadrupole magnets (see Sec. 3.3). The estimated beam spot sizes meet the requested design values for experiments at higher energies as the machine was optimised for the beams in the range 5.5 to 10 MeV/u.

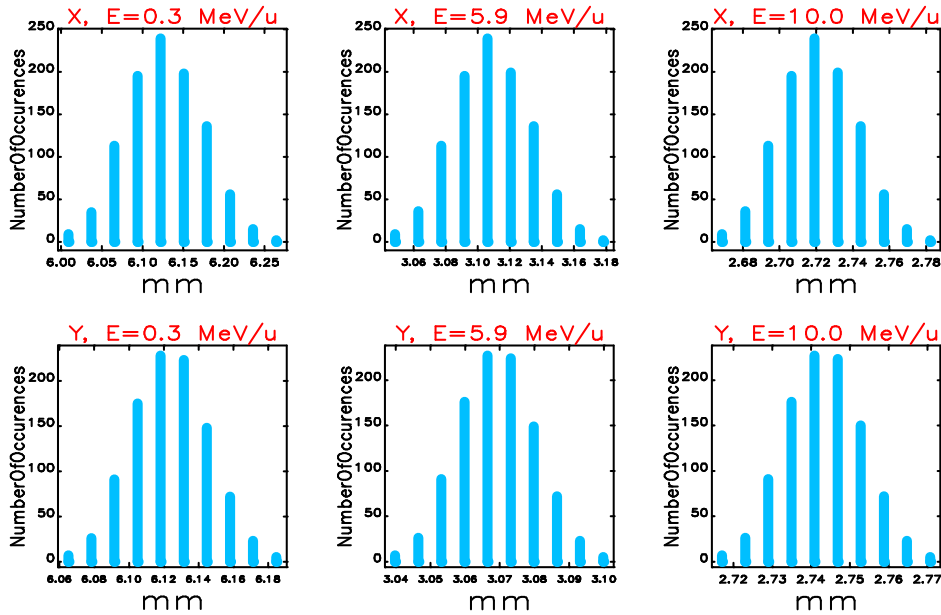
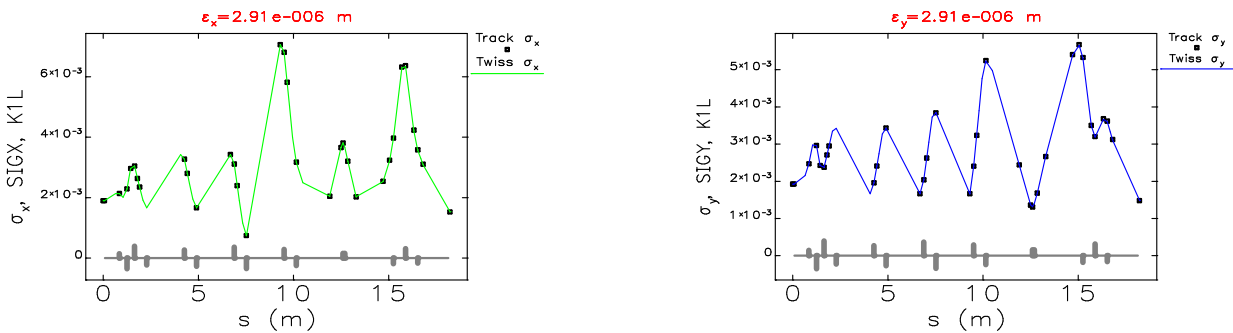


Figure 16: Estimated X-/Y- beam spots equal to $\pm 2\sigma$ (4σ) at the target for different energies obtained after *piecewise* trajectory correction of all static errors in 1000 seeds simulation.

3.5 Beam transmission at 0.3 MeV/u

3.5.1 Particle tracking vs. twiss

Tracking of the particle distribution was done with `ptc_track` module of MADX [3]. Beam sizes calculated from Twiss parameters by using beam parameters for 0.3 MeV/u of Table 4 in Sec. 7.5 (solid line) and from tracking (dots) are in agreement for both X-/Y- planes (Fig. 17) that shows that particle dynamics is very well represented by the linear optics.



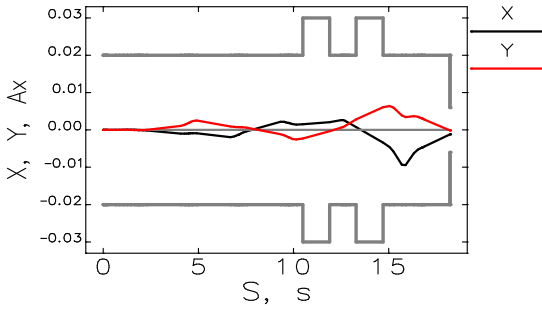
(a) X- plane

(b) Y- plane

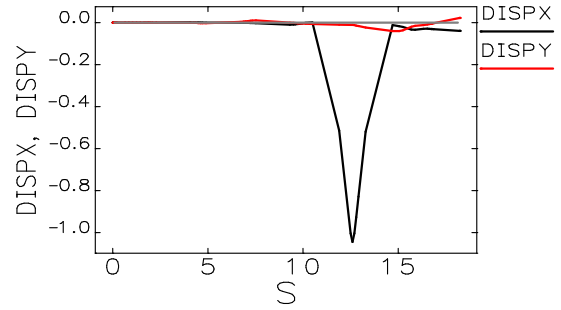
Figure 17: *One sigma* beam sizes $\sigma_{x/y}$ of Eq. (1) calculated from Twiss (solid line) and from tracking (dots) for both X-/Y- planes, respectively (*ideal trajectory*).

3.5.2 Accuracy of the linear optics approximation

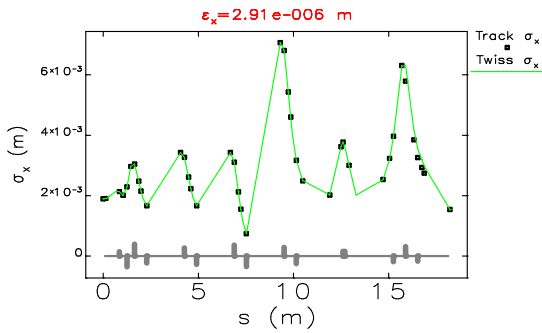
Usage of the beam sizes from Twiss parameters are justified by the following examples shown in Fig. 18. X-/Y- trajectories were distorted within *maximum corrected orbit distortion* (Fig. 15) and no beam loss was obtained even in presence of nonlinearities, which are very weak for that matter (see Sec. 7.7). An excellent agreement between particle tracking and Twiss optics is obtained.



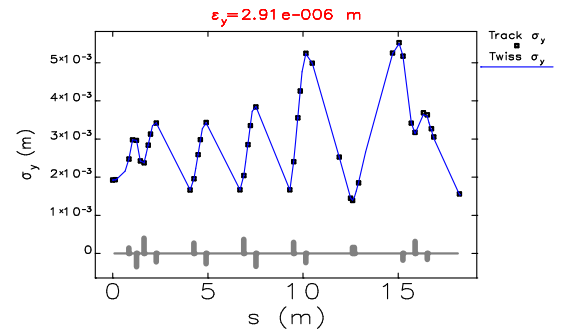
(a) X-/Y- trajectories



(b) Dispersion function



(c) X- plane



(d) Y- plane

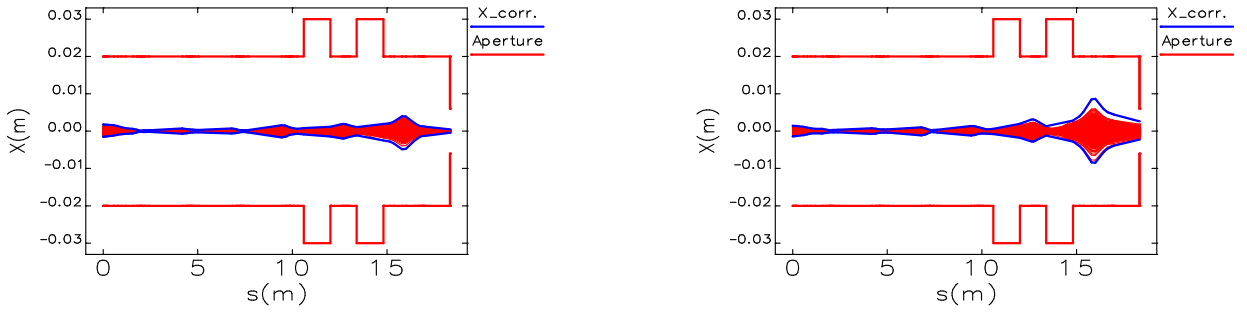
Figure 18: (top) X-/Y- trajectories distorted within maximum corrected orbit distortion in presence of nonlinearities and (bottom) corresponding X-/Y- beam sizes calculated from Twiss (solid line) and from tracking (dots).

Large trajectory distortions perturb the dispersion function. Note that a vertical dispersion could be generated by a vertical trajectory distortion. If there is a beam loss the beam sizes must be calculated only via tracking. If there is no beam loss (see Fig. 20) then Twiss parameters are sufficient to get an accurate beam sizes for the whole beam line.

3.5.3 Beam transmission for many error seeds

Particle distribution and beam parameters are presented in Sec. 7.5. Results on beam transmission for *an ideal trajectory* are presented in Sec. 7.6.

A tracking simulation with `ptc_track` of collimated distribution (lattice with apertures) for many error seeds was carried out (see MADX syntax details in Sec. 7.2.2). Introduced static errors were corrected. Dynamic errors at 0.3 MeV/u [Fig. 12 (b)] were introduced on top of the correction. Thus, particles were tracked for trajectories shown in Fig. 19 (b) for 300 seeds.



(a) All static errors corrected

(b) With dynamic errors in addition

Figure 19: Trajectories after global trajectory correction of all static errors and with dynamic errors added [see also the beam envelopes shown in Fig. 15 (a)].

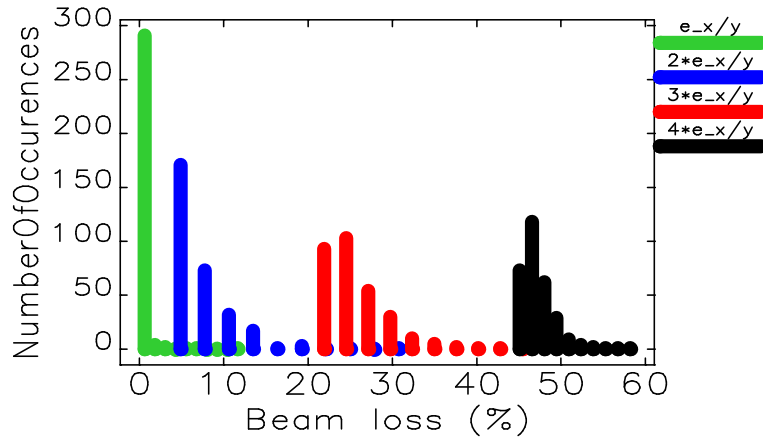
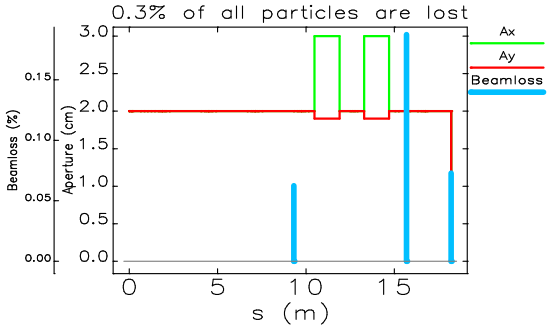


Figure 20: Beam transmission histogram as a function of the beam emittance for 300 error seeds.

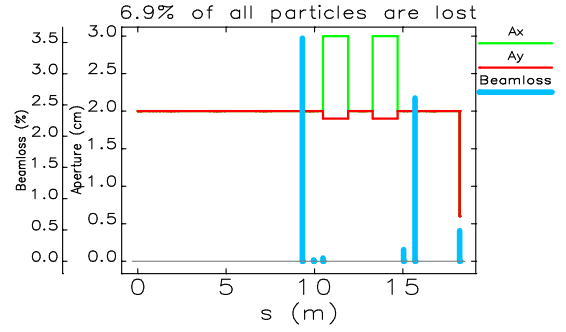
To study the dependence of beam loss on beam emittance, larger beams were produced from the original particle distribution at 0.3 MeV/u (Fig. 35) in Sec. 7.5 by multiplying the coordinates (x, x', y, y') by $\sqrt{2}$, $\sqrt{3}$ and $\sqrt{4}$, sequentially. Transmission histograms as a function of the beam emittance for 300 error seeds are plotted in Fig. 20.

The beam loss along the beam line averaged over 100 error seeds for several beams ($\epsilon_{x/y}$, $2\epsilon_{x/y}$, $3\epsilon_{x/y}$ and $4\epsilon_{x/y}$) is presented in Fig. 21. A reasonably low average beam loss of 0.3% was found for the original particle distribution with the nominal emittance of $\epsilon_x = 2.91 \cdot 10^{-6}$ m, $\epsilon_y = 2.91 \cdot 10^{-6}$ m. For the double and triple beam emittances the average beam loss found is 6.9% and 25.3%, respectively.

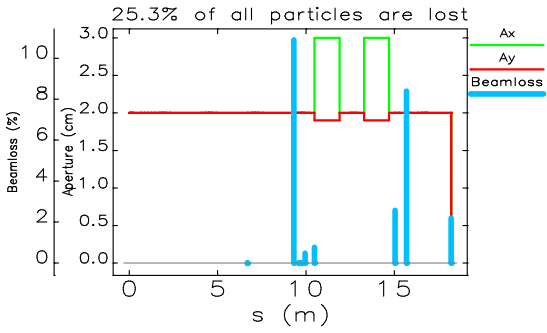
Fig. 22 demonstrates a well matched beam optics at 5.9 MeV/u. The beam sizes are smaller than those at the low energy (Fig. 17). A negligible total beam loss is found at 5.9 MeV/u for the nominal emittance.



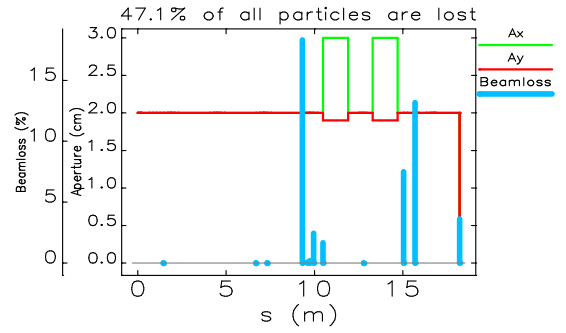
(a) $\epsilon_{x/y}$



(b) $2\epsilon_{x/y}$

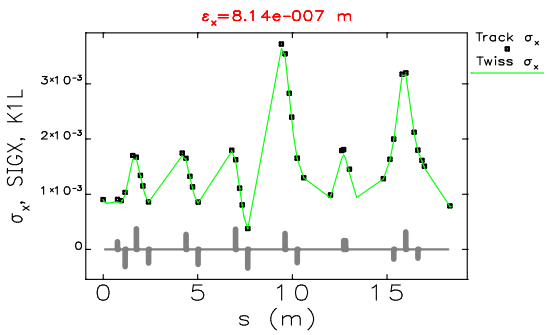


(c) $3\epsilon_{x/y}$

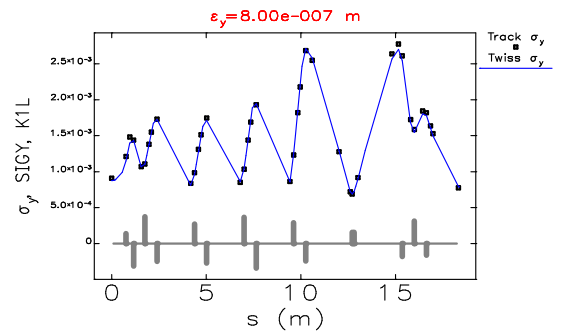


(d) $4\epsilon_{x/y}$

Figure 21: Beam loss distribution along the beam line averaged over 100 error seeds: $\epsilon_{x/y}$ - 0.3%, $2\epsilon_{x/y}$ - 6.9%, $3\epsilon_{x/y}$ - 25.3% and $4\epsilon_{x/y}$ - 47.1%.



(a) X- plane



(b) Y- plane

Figure 22: One sigma beam sizes $\sigma_{x/y}$ of Eq. (1) calculated from Twiss (solid line) and from tracking (dots) for both X-/Y- planes, respectively (*ideal trajectory*).

3.6 Bunch length estimates at the experiments

Experiments request 3 ns bunch length at the target.

Thus we define rms of the time coordinate (bunch duration) dt [ns] as a bunch length

$$s = t \cdot v, \quad \frac{dt}{t} = -\frac{dv}{v}, \quad dt = -\frac{s}{v} \cdot \frac{dv}{v}. \quad (2)$$

Particle velocity is equal to

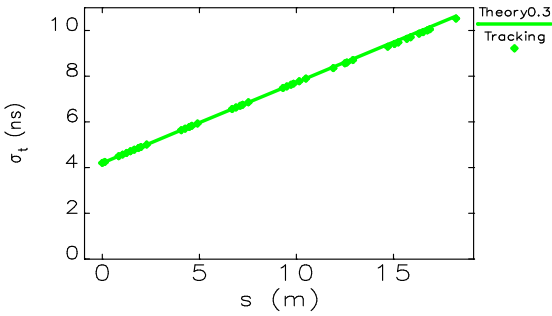
$$v = \beta c \approx c \cdot \sqrt{\frac{2W}{u}}, \quad (3)$$

where W is kinetic energy per nucleon in MeV/u and u is atomic mass $u = 931.494$ MeV/u. The derivative of Eq. (3) is

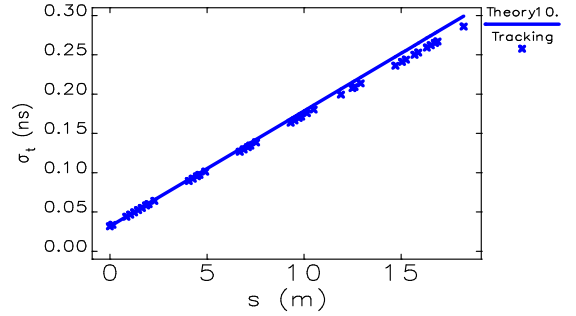
$$dv = c \cdot \frac{dW}{\sqrt{2uW}}. \quad (4)$$

Eqs. (2) and (4) give the lengthening of the bunch after the linac

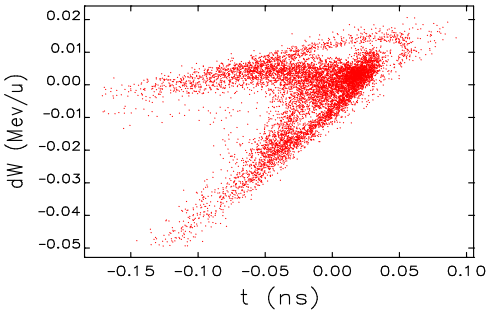
$$dt = \sigma_t = -\frac{s}{2v} \cdot \frac{dW}{W} = -\frac{s}{2\beta c} \cdot \frac{dW}{W}. \quad (5)$$



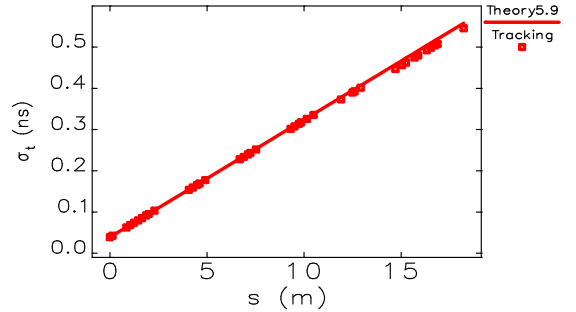
(a) 0.3 MeV/u



(b) 10 MeV/u



(c) 5.9 MeV/u (t-dW)-cut



(d) 5.9 MeV/u

Figure 23: Lengthening of the bunch in the HEBT. Bunch length σ_t is defined as one sigma.

The bunch length at the beginning of the HEBT for beams of different energies are in given in Table 4. The increase of the bunch length (lengthening of the bunch) until the XT01 target (18.21 m) is shown in Fig. 23. For higher energy beams the debunching effect is less both because the relativistic beta is larger

and the relative energy spread is also smaller on exit from the linac (see Table 4). According to Fig. 23 the bunch length increase until the target of XT01 is 6.32 ns at 0.3 MeV/u, 0.6 ns at 5.9 MeV/u and 0.3 ns at 10 MeV/u. Note that at 5.9 MeV/u the particle beam is strongly non-symmetric (and not elliptical) due to 9-GAP IH [Fig. 36 (d)]. The tails of the original distribution were cut as in Fig. 23 (c) after the fitting and particle tracking were performed.

Remark: All cavities are used to get the maximum energy and none are used to rebunch the beam at the experiment, which could be done at energies above approximately 3 MeV/u.

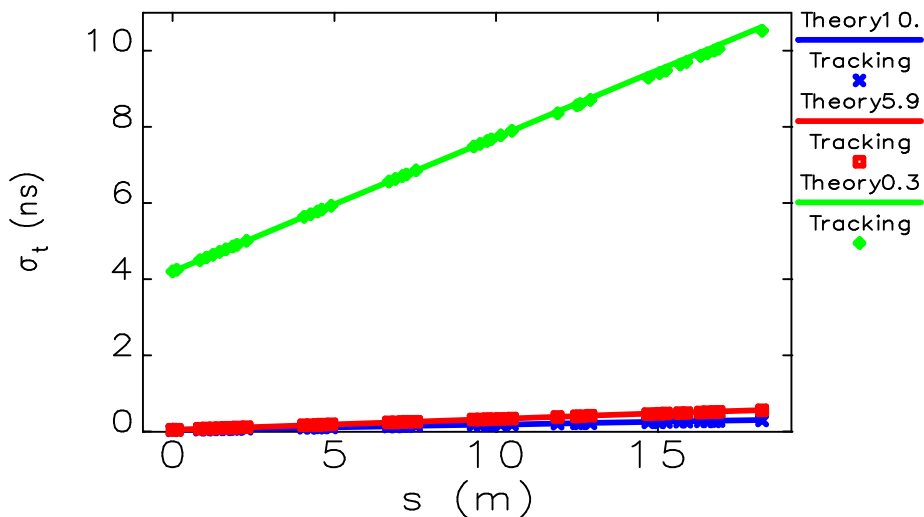


Figure 24: Lengthening of the bunch in the HEBT at 0.3, 5.9 and 10 MeV/u.

4 Conclusion and Outlook

Errors of different types have been considered and their effects on the machine have been studied and corrected. Tolerances on field quality and magnet alignment were specified. It was shown that a trajectory distortion generated by *all static errors* can be corrected and steerer strengths used in the correction were determined. Correction of particle offset and angle at the target (*orthogonal steering*) was demonstrated and the ranges of the target offset were defined.

Estimated average X-/Y- beam spots at the target defined as 4σ are about 2.7 mm at 10 MeV/u; 3 mm at 5.9 MeV/u and 6 mm at 0.3 MeV/u, which meet the requested design values for experiments at higher energies. At the low energy (0.3 MeV/u) dynamic errors introduce a dilution of X-beam spot at the target with a sigma of 0.3 mm.

The beam transmission at 0.3 MeV/u was studied in detail. It was demonstrated that twiss optics coincides with beam optics calculated from particle tracking. The remaining acceptance is about 2.5σ for X and 3.0σ for Y sufficient for the beam transmission.

Particle tracking with many error seeds and different beam emittances was carried out. *A reasonably low average beam loss* of 0.3% at 0.3 MeV/u and less than 0.1% at 5.9 MeV/u was found for the nominal emittance. For the double and triple beam emittance the average beam loss found is 6.9% and 25.3%, respectively.

Bunch lengthening until the target of XT01 (18.21 m) is 6.32 ns at 0.3 MeV/u, 0.6 ns at 5.9 MeV/u and 0.3 ns at 10 MeV/u.

5 Acknowledgement

The authors thank W. Herr, A. Petrenko, G. Franchetti, L. Dienau, F. Schmidt and W. Bartmann for scientific discussions, programming tips and benchmarking of MadX tools.

6 References

- [1] D. Voulot et al., “HIE-ISOLDE SC Linac: Operational Aspects and commissioning preparation”, IPAC’2012, New Orleans, Louisiana, USA, THPPP050, p. 3853 (2012).
- [2] A. Parfenova et al., “Design and performance of the beam transfer lines for the HIE-ISOLDE project”, IPAC’2013, Shanghai, China, MOPFI059 (2013).
- [3] F. C. Iselin, *The MAD Program, Methodical Accelerator Design*, CERN, Geneva, Switzerland, 2000, <http://mad.web.cern.ch/mad/>.
- [4] K. R. Crandall et al., *TRACE 3-D Documentation*, Los Alamos National Laboratory, New Mexico, USA, 1997, <http://laacg1.lanl.gov>.
- [5] M. A. Fraser, *Beam Dynamics Studies of the ISOLDE Post-accelerator for the High Intensity and Energy Upgrade*, PhD Thesis, Manchester, U.K., 2012, 167, <https://www.escholar.manchester.ac.uk/api/datastream?publicationPid=uk-ac-man-scw:155665&datastreamId=FULL-TEXT.PDF>.
- [6] M. A. Fraser, “Notes on the HIE-ISOLDE HEBT”, HIE-ISOLDE-PROJECT-Note-0013, CERN, Switzerland, October 2011, <https://cds.cern.ch/record/1436078?ln=en>.
- [7] S. Y. Lee, *Accelerator Physics*, World Scientific, Singapore, 2004, 85.
- [8] M. Borland et al., “The Self-Describing Data Sets File Protocol and Program Toolkit”, Proc. ICALEPCS 1995, Chicago, Illinois, USA, pp. 653 (1996), <http://www.aps.anl.gov/asd/oag/software.shtml>.
- [9] HEBT beam optics simulations, DFS space, G:\Departments\BE\Projects\HIE-ISOLDE\HIE-REX\Beam_simulations.
- [10] Lyman R. Ott, Michael Longnecker, *An Introduction to Statistical Methods And Data Analysis*, p.95 Empirical rule.
- [11] E. Forest et al., *Introduction to the Polymorphic Tracking Code*, CERN-KEK 2002, **page 72**, http://madx.web.cern.ch/madx/doc/ptc_intro.pdf.
- [12] http://www.aps.anl.gov/Accelerator_Systems_Division/Accelerator_Operations_Physics/manuals/elegant_ver17.1.1/node65.html.
- [13] J. Bauche, “HIE-ISOLDE Technical Design Review 2012”, CERN, Geneva, Switzerland, <https://indico.cern.ch/getFile.py/access?contribId=2&resId=1&materialId=slides&confId=194310>.
- [14] V. Kapin, G. Franchetti, “The SIS100 Dipole and Quadrupole integrated kicks for nonlinear components”, GSI internal report, Darmstadt, Germany, <http://www-alt.gsi.de/documents/DOC-2010-Jul-289-1.pdf>.

7 APPENDIX

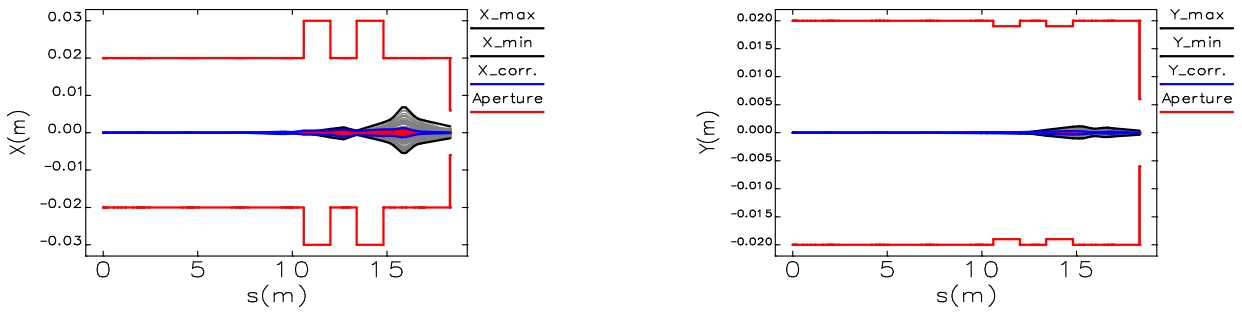
7.1 Individual static error sources

Below each static error-source considered separately, whose tolerances are listed in Table 1. The MADX syntax for each error source is documented.

7.1.1 Dipole errors

Dipole field $\Delta Bdl/Bdl$, roll angle $d\psi$ and longitudinal position dS are included as dipole errors. Due to the coupling introduced by dipole roll angle $d\psi$ (Fig. 25) the vertical trajectory is slightly distorted. The reference radius is $R_{ref} = 20$ mm (see Sec. 7.7.1).

```
EALIGN, dps:= (2*ranf()-1.0)*1.0e-4, ds:= (2*ranf()-1.0)*1.0e-3;
md.error:= (2*ranf()-1.0)*1.0e-3;
EFCOMP, ORDER:=0, RADIUS:= 0.02, DKNR:=md.error,0,0,0;
select, flag=error, class="rbend";
eprint; esave;
```



(a) X- plane

(b) Y- plane

Figure 25: Trajectories before and after correction in presence of dipole errors.

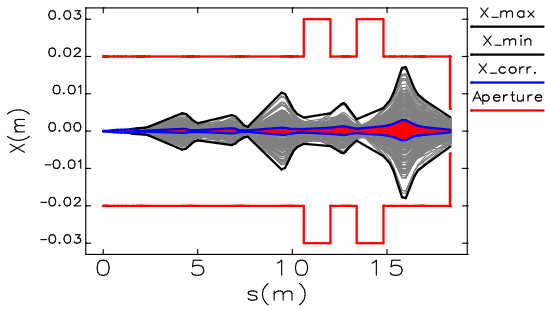
7.1.2 Quadrupole errors

```
select, flag=error, clear;
q1.error:=1.0e-3*(2*ranf()-1.0);
EFCOMP, ORDER:=1, RADIUS:=0.02, DKNR:=0,q1.error,0,0,0;
EALIGN, dx := 2.5e-4*TGAUSS(2.4), dy:=2.5e-04*TGAUSS(2.4);
select, flag=error, class="quadrupole";
eprint; esave;
```

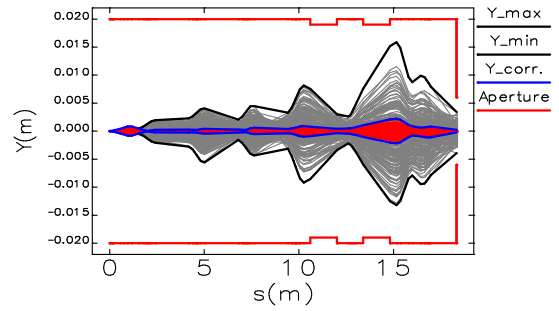
7.1.3 Initial conditions

The following parameters need to be specified in TWISS command

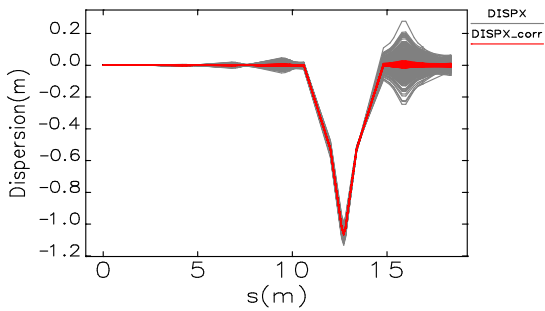
```
x = [tx] = 0.5e-3*tgauss(4.);
x = [tpx] = 0.5e-3*tgauss(4.);
y = [ty] = 0.5e-3*tgauss(4.);
py = [tpy] = 0.5e-3*tgauss(4.);
```



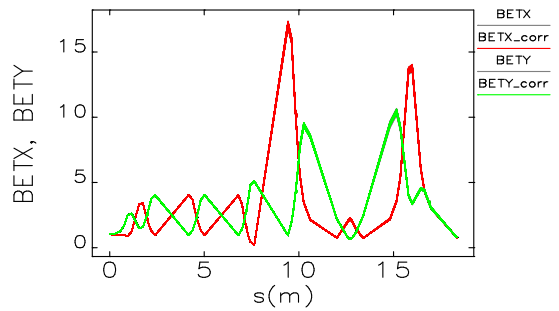
(a) X- plane



(b) Y- plane

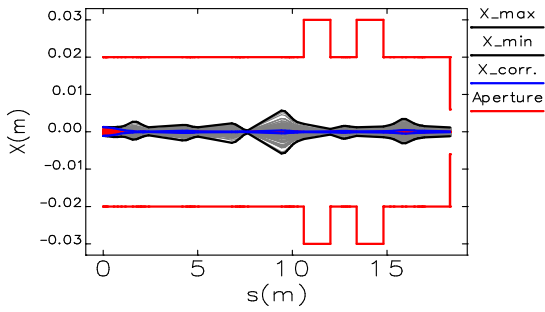


(c) dispersion

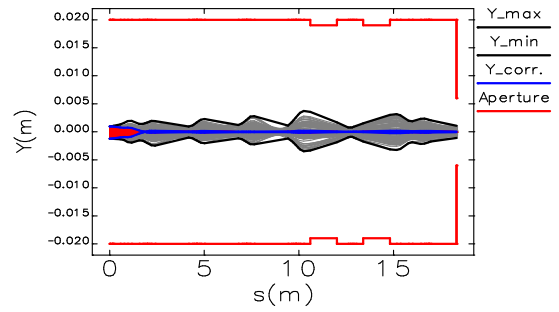


(d) β -functions

Figure 26: Trajectories before and after correction, dispersion and β -functions in presence of quadrupole errors



(a) X- plane



(b) Y- plane

Figure 27: Trajectories before and after correction in presence of divergence on entering the HEBT (initial conditions).

7.1.4 Malfunction of beam position monitors

Monitor's (diagnostic boxes) alignment in both X-/Y- planes and its' accuracy (resolution) is introduced

```
select, flag=error, clear;
EALIGN, dx:=0.25e-3*tgauss(2.4), dy:=0.25e-3*tgauss(2.4),
MREX=200E-06*(2*ranf()-1.0), MREY=200E-06*(2*ranf()-1.0);
select, flag=error, class="monitor";
```

```
eprint; esave;
```

In order to include monitor *malfunction* (failure) of monitors, for example 20%, an option `MONON=0.8` has to be included into `CORRECT` command. Monitor malfunction degrades the trajectory correction (Fig. 28).

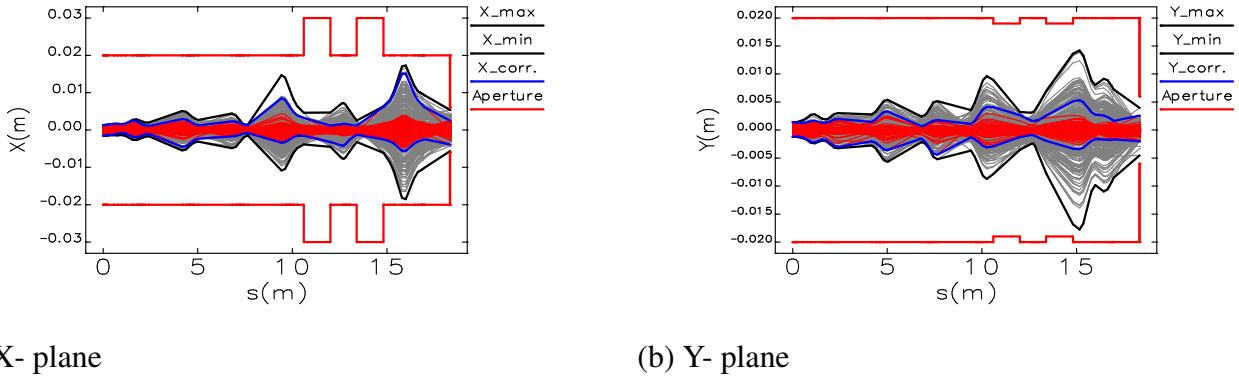


Figure 28: Monitor malfunction added on top to *all static errors* for the original simulation presented in Fig. 4.

7.1.5 Remnant field considerations

Remnant field for lines XT02 and XT03 can be estimated by introducing an extra dipole with zero length via

```
select, flag=error, clear;
select, flag=error, pattern="DB20";
md.error:=-1.26e-3;
where DB20: RBEND, L=0.67, ANGLE=0.
```

Remark: However, there is no more issue about dipole remnant field since the magnetic field will be measured on-line on each dipole. The magnet current shall be regulated according to this measurement. The power converters being 4-quadrants, so that the remnant field is automatically compensated by this system [13].

7.2 TRACE3D to MADX conversion: major aspects

TRACE3D quadrupolar gradients need to be scaled with the rigidity ($B\rho$) while converting to MADX

```
real const Brho = ion_energy*1.0e+9*beta_rel/Q/300.0*1.0e-4*1.0e-2; ! in T*m
```

```
XT00.MQ30: QUADRUPOLE, L=0.2, K1=17.059655/(Brho),
```

where `ion_energy` in `BEAM` command is specified as follows

```
ER = 41917.2435;
```

```
Q = 10;
```

```
W = 265.5; ! in MeV = 5.9*A full kinetic energy
```

```
u = 931.494;
```

```
A = ER/u;
```

```
ion_mass = 41917.2435/1000; ! in GeV
```

```
E.k = 265.5/1000; ! in GeV
```

```
gamma_rel = W/(A*u) + 1; ! relativistic gamma
```

```
beta_rel = sqrt(1 - 1/(gamma_rel)^2); ! relativistic beta
```

```
ion_energy = ion_mass + E.k;
BEAM, particle = ion, mass = ion_mass, energy = ion_energy, charge = Q;
After the conversion to MADX the dispersion in the achromat is closed using the TRACE3D quadrupolar gradients scaled with the rigidity.
```

For RBEND dipole magnets the following quantities have to be considered in MADX as they are considered in TRACE3D: HGAP=0.025, FINT=0.55.

```
Note that in order to calculate the length of the RBEND dipole correctly the RBARC has to be turned off
option, RBARC = FALSE; ! // use arc length of RBENDS
XT01.MD10: RBEND, L = 1.4137167, ANGLE = -pi/4.0, K0 = -(pi/4.0)/1.4137167,
HGAP = 0.025, FINT = 0.55;.
```

Note that K0 needs to be specified for both types RBEND and SBEND magnets for the assignment of field errors in EFCOMP command [3].

7.2.1 Steffen's matrix

It is important to match the beam in MADX the same way as it is done in TRACE3D. Thus, the same as used in TRACE3D initial conditions for α_{x0} , α_{y0} , β_{x0} and β_{y0} should be included in the TWISS command. The beam line also must start at the same position.

TRACE3D simulation starts at 250 mm after the last cavity. This does not allow to include properly steerer XLI4.ST20 in the MADX lattice. For this reason the beam line must be drifted backwards on $L = 0.11$ m and the initial beam parameters need to be recalculated. The evolution of the betatron amplitude function in a drift space is [7] (page 51)

$$\begin{aligned}\beta_2 &= \frac{1}{\gamma_1} + \gamma_1 \left(s - \frac{\alpha_1}{\gamma_1}\right)^2 = \beta^* + \frac{(s - s^*)^2}{\beta^*}, \\ \alpha_2 &= \alpha_1 - \gamma_1 s = -(s - s^*)/\beta^*, \\ \gamma_2 &= \gamma_1 = 1/\beta^*,\end{aligned}\tag{6}$$

Note that $\gamma = \gamma_1 = \gamma_2$ is constant in a drift space, and $s^* = \alpha_1/\gamma_1$.

TRACE3D initial beam parameters (location "1"):

```
alphax0=0.270; betax0=1.000; alphay0=-0.040; betay0=1.030
```

MADX version 6 initial beam parameters (location "2"):

```
alphax0=0.38802; betax0=1.0738; alphay0=0.06697; betay0=1.03297
```

7.2.2 Ptc_track syntax

Conversion of particle distribution for ptc_track command

Built into MADX ptc_track command is called using following syntax:

```
ptc_create_universe;
ptc_create_layout, model = 2, method = 6, nst = 10, exact;
call file = "beam.madx";
ptc_observe, place = MASHINE$START;
ptc_observe, place = ..... ;
.....
ptc_observe,place = MASHINE$END;
ptc_track, time= true, icafe = 6, turns = 1, ffile = 1, onetable,
ELEMENT_BY_ELEMENT, file='results/track',dump;
```

File beam.madx contains initial particle distribution for ptc_start command according to MADX canonical variables [3, 11] and is obtained from file coord4.out by the following transformation of its columns

```
ptc_start, x = column5/1.0e+2, y = column7/1.0e+2,
px = column6/(1.0e+3+column4/1.0e+3*A/beta_rel/ion_energy),
py = column8/(1.0e+3+column4/1.0e+3*A/beta_rel/ion_energy),
t = column3*1.0e-9*3.0e+8*(-1.0), pt = column4/1.0e+3*A/beta_rel/ion_energy;
where ion_mass and ion_energy are defined in the previous section; in coord4.out: column3 is dt[nsec], column4 is dW[Mev/u], column5 is x[cm], column6 is x'[mrad], column7 is y[cm], column8 is y'[mrad].
```

Errors' assignment in ptc_track command

There is a possibility that ptc_track recognizes assigned alignment and field errors by calling error-file and using align command:

```
eoption, add=false, seed=22021474;
call, file='miniball_errors.madx';
ptc_align;
```

Aperture treatment in ptc_track command

Beam apertures can be assigned in the lattice itself

```
XT00.MQ10: QUADRUPOLE, L = 0.2, K1 = 5.8989801/(brho), apertype = circle,
APERTURE = {0.02,0.02};
```

In this case exact apertures are assigned to all elements. The assigned apertures are printed out in tables TWISS and PTC_TWISS. Note that MADX does not assign apertures to DRIFT elements [3].

There exist an alternative option MAXAPER in ptc_track for a lattice without apertures, i.e. no APERTURE assigned to a lattice element. MAXAPER provides an estimate of the beam loss by assigning constant aperture limits to the complete beam line (*upper limits for the six coordinates*):

```
ptc_track, icode = 6, turns = 1, ffile = 1, onetable, ELEMENT_BY_ELEMENT,
MAXAPER = {0.02,0.01,0.02,0.01,0.0,0.0}, file = 'results/track', dump;
```

Note that MAXAPER command is less precise than using lattice with apertures and can be used for a rough beam loss estimate [3].

7.2.3 Orthogonal steering MADX syntax

The orthogonal steering correction is done by MATCH and CONSTRAINT commands in MADX with the following syntax for matching in X- plane

```
alphax0 = 0.388019; betax0 = 1.07382; alphay0 = 0.06697; betay0 = 1.03296;
match, sequence = machine, betx = betax0, alfx = alphax0,
dx = 0.0, dpx = 0.0, bety = betay0, alfy = alphay0, dy = 0.0, dpy = 0.0,
x = tx, px = tpx, y = ty, py = tpy;
! initial conditions drift [tx, tpx, ty, tpy] are considered as described
in Sec. 7.1.3
constraint, sequence = machine, range = #e, x = 0.0, px = 0.0;
! where #e is end of the sequence "machine", i.e. the target
VARY, NAME = var1, STEP = 0.00001;
```



```

VARY, NAME = var2, STEP = 0.00001;
lmdif, calls = 200, tolerance = 1.e-8;
endmatch;
value, XT00.ST135->HKICK;
value, XT01.ST95->HKICK.

```

Note that `var1` and `var2` are variables used in `CONSTRAINT` command for the steerer strengths and are defined in the lattice sequence

```

XT00.ST135: steerer, HKICK := var1, VKICK := var3;
XT01.ST95:  steerer, HKICK := var2, VKICK := var4.

```

In Y- plane variables `var3` and `var4` are used. Note that `MATCH` command for a beam line (not a ring) requires specifying of the initial conditions.

7.3 Reduction of steerers and monitors

The actual baseline beam optics layout version 6 is presented in Fig. 1. Since all three branches are identical, the longest branch XT03 was studied for the case of the reduction of steerers and monitors. β -functions for XT03 are shown in Fig. 30. Piecewise trajectory correction for the complete number of

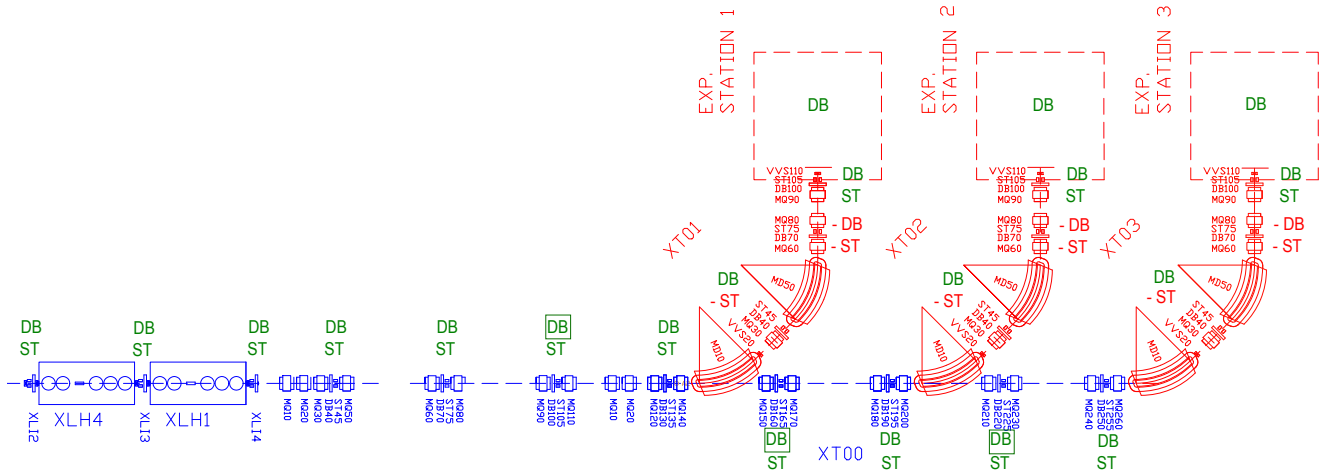


Figure 29: The baseline layout with three identical branches. Monitors (diagnostic boxes) are marked with DB and steerers with ST: removed (red with "-") and kept (green). Some of monitors marked with the green frame can not be removed because of the important diagnostics.

monitors and steerers (version 5) is shown in Fig. 31.

In order to measure and to correct well the trajectory the phase space advance between two consecutive devices must be equal to *one fourth of the betatron period*, namely,

$$\begin{aligned} \Delta\mu_x(i+1, 1) &= \frac{\pi}{2} = 0.25, \\ \Delta\mu_y(j+1, j) &= \frac{\pi}{2} = 0.25, \end{aligned} \quad (7)$$

where it is normalized on 2π in MADX units and indexes i, j enumerate monitors and steerers, respectively. If phase advance between two consecutive monitors (or steerers) is larger than $\pi/2$ an *uncorrectable unmeasurable local trajectory bump can be present in between*. If the phase advance is smaller than $\pi/2$ then monitors (or steerers) can become *redundant*. The phase advances between consecutive monitors and steerers for XT03 are shown in Fig. 32.

As can be seen in Fig. 32 both `XT03.ST75` and `XT03.DB70` can be removed, because of the small $\Delta\mu_x$

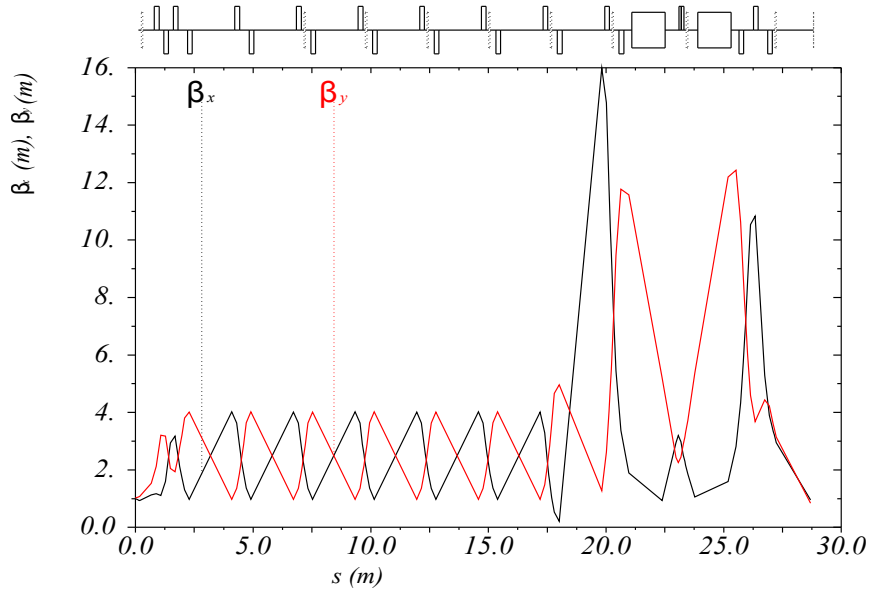
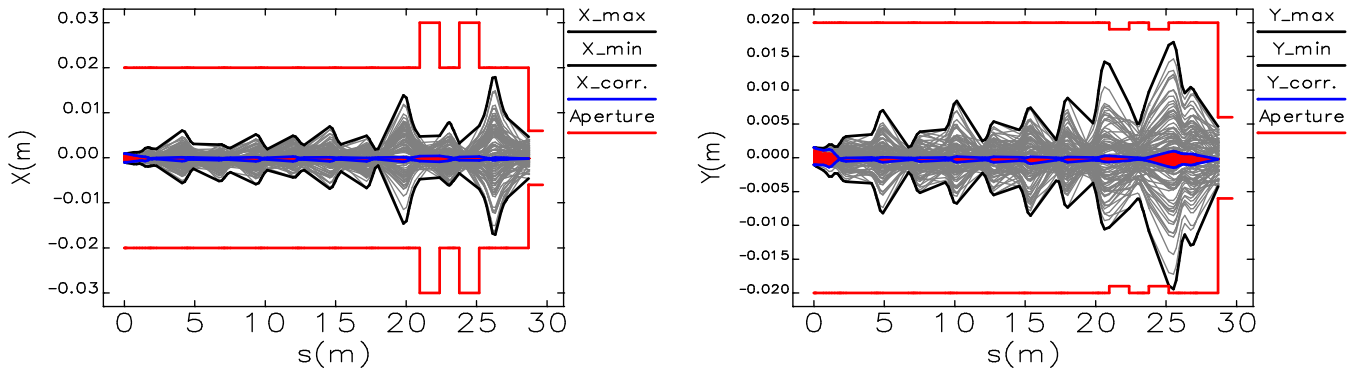


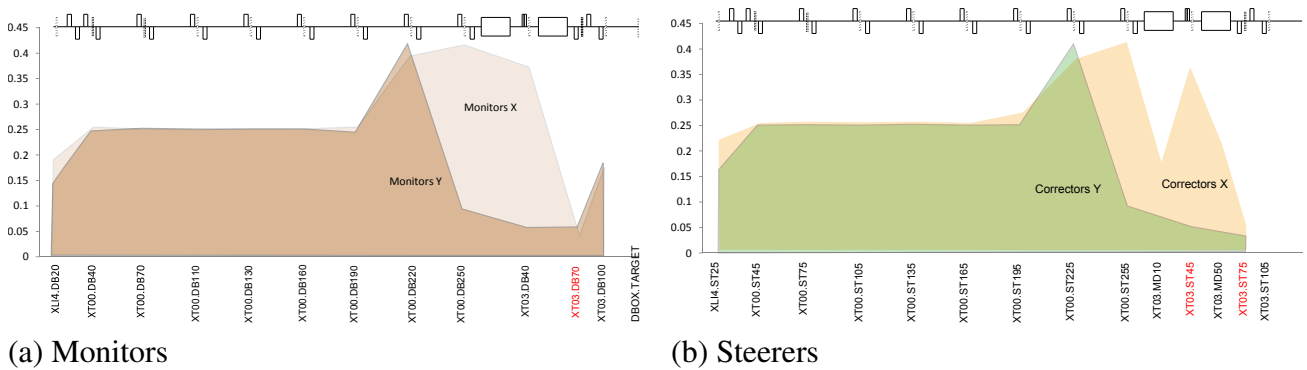
Figure 30: β -functions for XT03.



(a) X- plane

(b) Y- plane

Figure 31: Piecewise correction for XT03 using all originally planned monitors and steerers.



(a) Monitors

(b) Steerers

Figure 32: *Phase advance* between two consecutive monitors (a) and steerers (b) for XT03.

and $\Delta\mu_y$, which does not impact much the correction efficiency.

Steerer XT03.ST45 in the achromat can be removed as it has a small vertical $\Delta\mu_y$ and therefore redun-

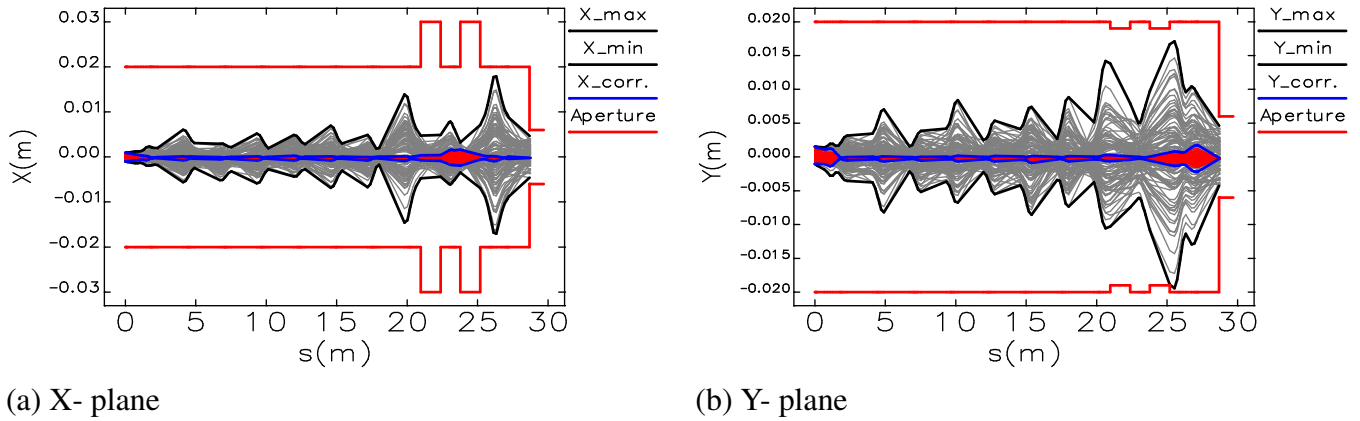


Figure 33: Piecewise correction for XT03 with one monitor and two steerers reduced.

dant in Y- plane (Fig. 32). In X-plane instead of it *horizontal steering with dipole magnets* XT03.MD10 and XT03.MD50 is possible.

Piecewise trajectory correction for the reduced number of monitors and steerers is presented in Fig. 33. *In total for the three beam lines there are $3 \times (2+1)$ devices less: six steerers and three monitors signed in red colour with "-" in Fig. 29.* It has been checked in simulation and as follows from Fig. 32 that further reduction of steerers and monitors in front of the achromats leads to unsatisfactory beam transmission.

7.4 Estimate of beam transmission via remaining acceptance

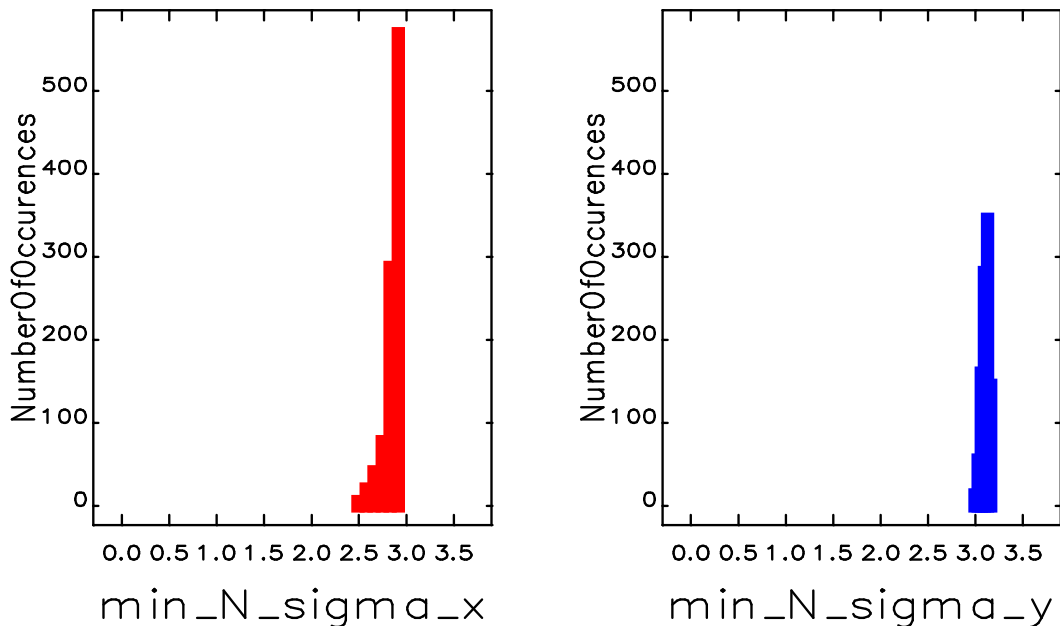


Figure 34: X-/Y- remaining acceptance estimated via the minimum number of one sigma beam sizes $\sigma_{x/y}$ in between the beam line aperture and the beam envelope at 0.3 MeV/u.

An alternative way of estimating beam transmission is to estimate how many beam sizes are fitted in between the beamline aperture and the maximum beam envelope. The remaining acceptance can be

estimated by the following Equation

$$N_{\sigma_{x/y}} = \frac{\text{APERTURE}(x/y) - \text{MAX_ENVELOPE}(x/y)}{\sigma_{x/y}}, \quad (8)$$

where maximum trajectory envelope MAX_ENVELOPE shown in Fig. 15 represents all static errors corrected and dynamic errors on top at 0.3 MeV/u.

In Eq. (8) MAX_ENVELOPE subtracted from the aperture APERTURE and divided by *one sigma beam size* along the beam line. Simulation for 1000 seeds is presented in Fig. 34. Fig. 34 shows that remaining aperture is always about 2.5σ for X and about 3.0σ for Y.

7.5 Particle distributions: 0.3, 5.9 and 10 MeV/u (A/q=4.5)

Table 4: Parameters of the particle distributions in Figs. 35, 36 and 37.

W, MeV/u	0.3	5.9	10
particles	9614	9256 (9049)	9614
ϵ_x , m	$2.91 \cdot 10^{-6}$	$0.749 \cdot 10^{-6}$	$0.574 \cdot 10^{-6}$
ϵ_y , m	$2.91 \cdot 10^{-6}$	$0.731 \cdot 10^{-6}$	$0.584 \cdot 10^{-6}$
α_x	$6.46 \cdot 10^{-3}$	0.346	-0.502
β_x , m	1.24	1.03	2.22
α_y	$1.82 \cdot 10^{-3}$	$3.39 \cdot 10^{-3}$	-0.34
β_y , m	1.27	1.05	1.26
$\epsilon_{x,norm}$, m	$7.39 \cdot 10^{-8}$	$8.44 \cdot 10^{-8}$	$8.43 \cdot 10^{-8}$
$\sigma_{\Delta p/p}$	$2.68 \cdot 10^{-3}$	$1.09 \cdot 10^{-3}$	$0.641 \cdot 10^{-3}$
bunch length dt , ns	4.2	$4.27 \cdot 10^{-2}$ ($3.88 \cdot 10^{-2}$)	$3.17 \cdot 10^{-2}$
dW , MeV/u	$1.61 \cdot 10^{-3}$	$7.32 \cdot 10^{-2}$ ($1.13 \cdot 10^{-2}$)	$1.28 \cdot 10^{-2}$
dW/W , %	5.4	1.2	0.12

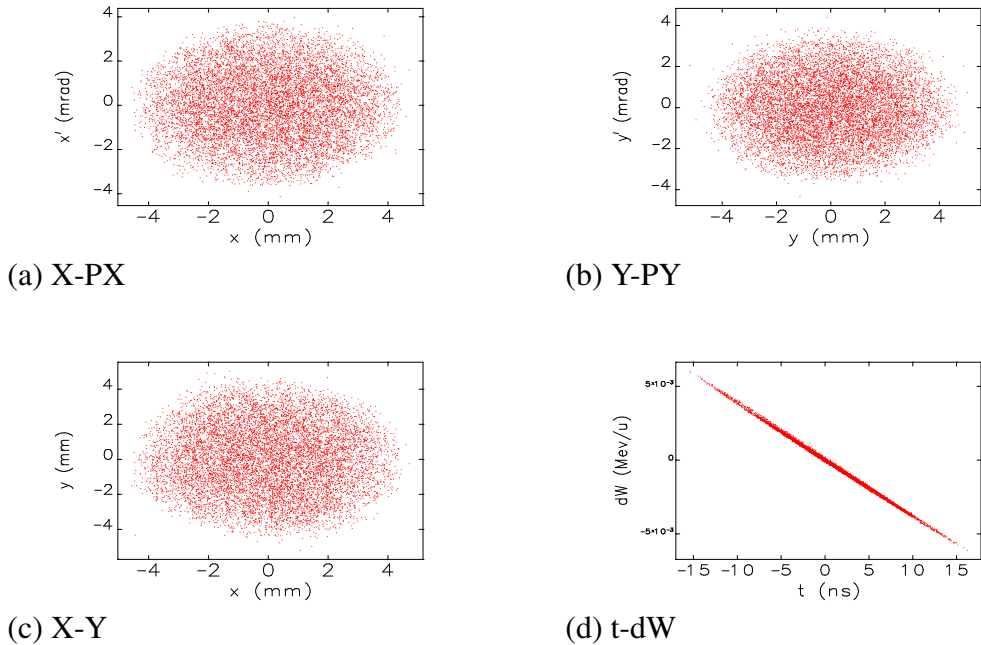


Figure 35: Initial particle distribution at 0.3 MeV/u, file coord4.out [5].

Initial particle distributions at the linac exit (right after the last cavity) are presented in Fig. 35 at 0.3 MeV/u, in Fig. 36 at 5.9 MeV/u and in Fig. 37 [5] at 10 MeV/u. Parameters of the particle distributions for the tree energies are given in Table 4, the data analysis was done using sddsanalyzebeam [12] program from the SDDS-toolkit [8].

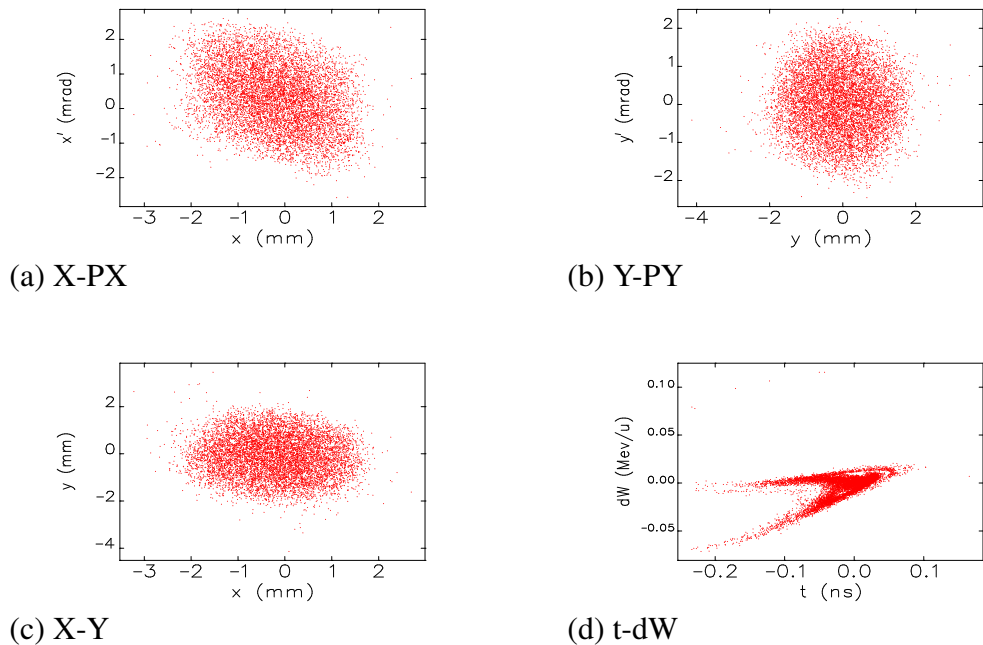


Figure 36: Initial particle distribution at 5.9 MeV/u [5].

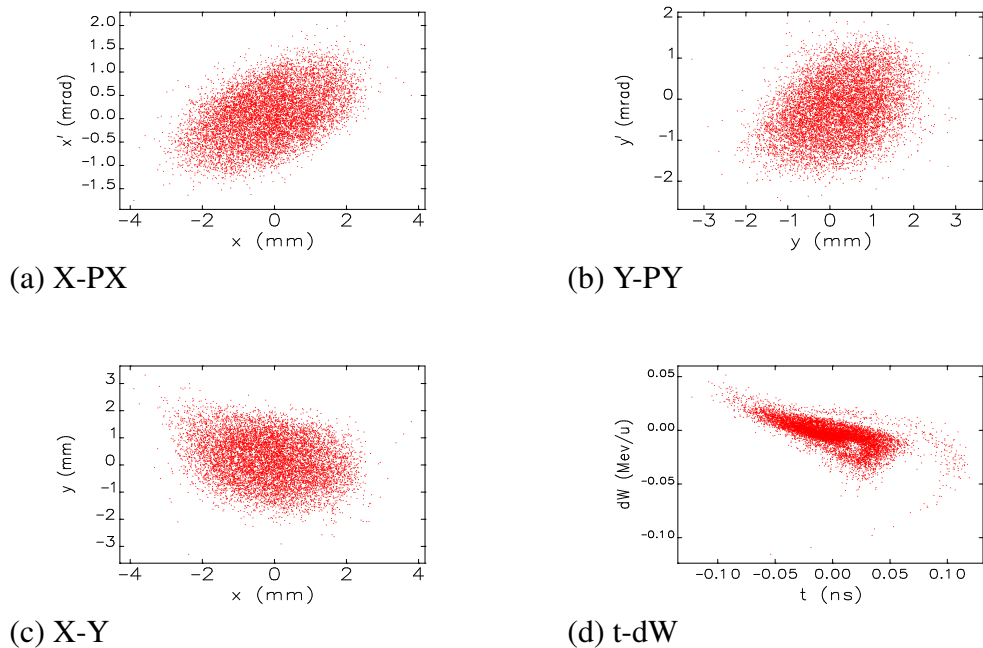


Figure 37: Initial particle distribution at 10 MeV/u [5].

7.6 Beam transmission at 0.3 MeV/u: benchmarking of ptc_track collimation

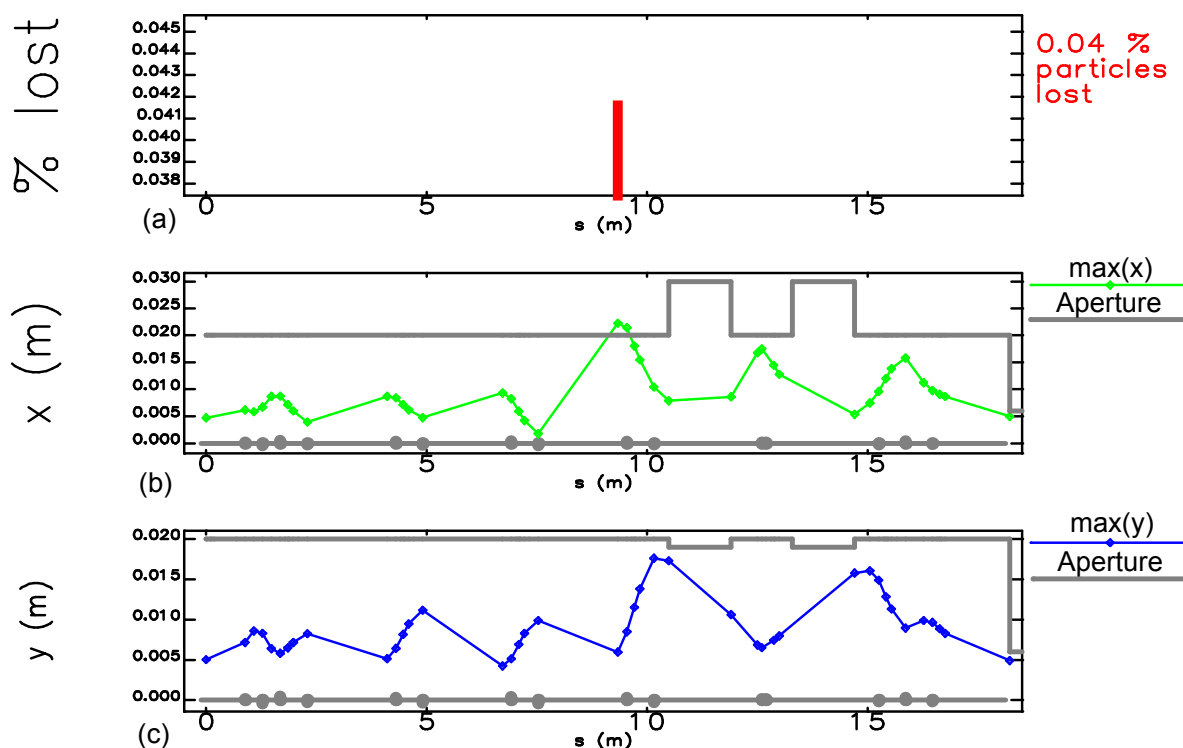


Figure 38: Beam transmission for an ideal trajectory (one seed).

Beam losses along the beam line were obtained in post analysis of `ptc_track` output in following steps: (1) output uncollimated distribution along the beam line, (2) apply aperture collimation at each observation point (compare particle coordinates with the aperture at each watch point), (3) save lost particles in separate file, (4) remove duplicated collimations.

Results for one seed (machine) without trajectory distortion (ideal trajectory) are presented in Fig. 38. Particle beam loss obtained in Fig. 38 (a) is 0.04 %. Maximum X-/Y- envelopes are presented in Fig. 38 (b) and (c), respectively. The uncollimated distribution (i.e. no MAXAPER command and lattice without apertures) was tracked and post-processed. MADX syntax details for `ptc_track` command are given in APP. 7.2.2.

The post analysis collimation was benchmarkd against `ptc_tracking` of the collimated distribution for several larger beams. Beams with larger emittance were produced from the original particle distribution at 0.3 MeV/u (Fig. 35) in Sec. 7.5 by multiplying the coordinates (x, x', y, y') by $\sqrt{2}, \sqrt{3}, \sqrt{4}, \sqrt{5}, \sqrt{6}$, respectively. Detailed beam loss distribution along the beam line for both ways of analysis is presented in Fig. 40. In Fig. 39 beam transmission for a machine with ideal trajectory as function of beam emittance is presented: both ways of data analysis demonstrated good agreement.

Remark: The benchmarking simulations were done with version 5 of the beam layout (XT01 line). For this reason minor differences in the beam losses compare to those in Sec. 3.5 are possible.

7.7 Magnets' nonlinear components

Nonlinear effects are mostly important at the low energy, where beam emittance and energy spread are large. Harmonic components for HIE-ISOLDE new magnets are listed in App. 7.7.4. Harmonics were

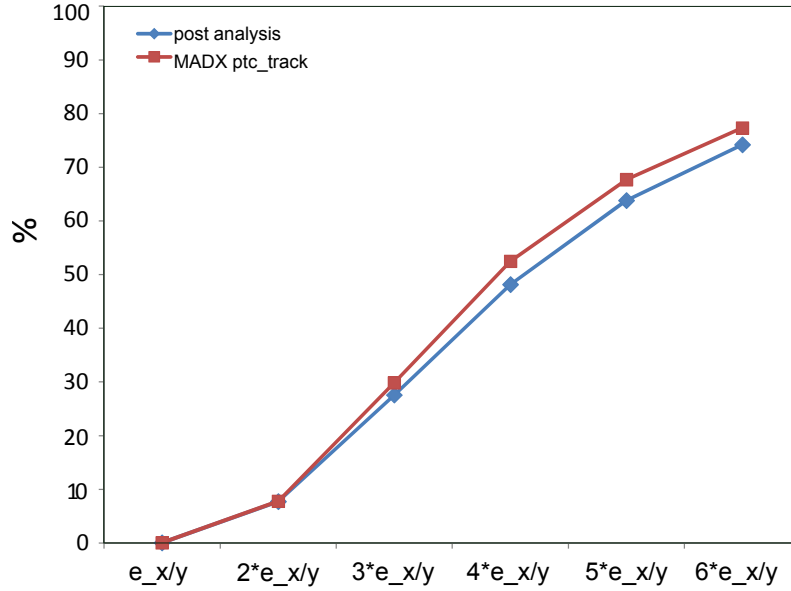


Figure 39: Beam transmission as a function of the beam emittance for an *an ideal trajectory* (one seed). Ptc_tracking of uncollimated distribution with the post-collimation (blue) and of collimated distribution (red) via setting lattice apertures in MADX.

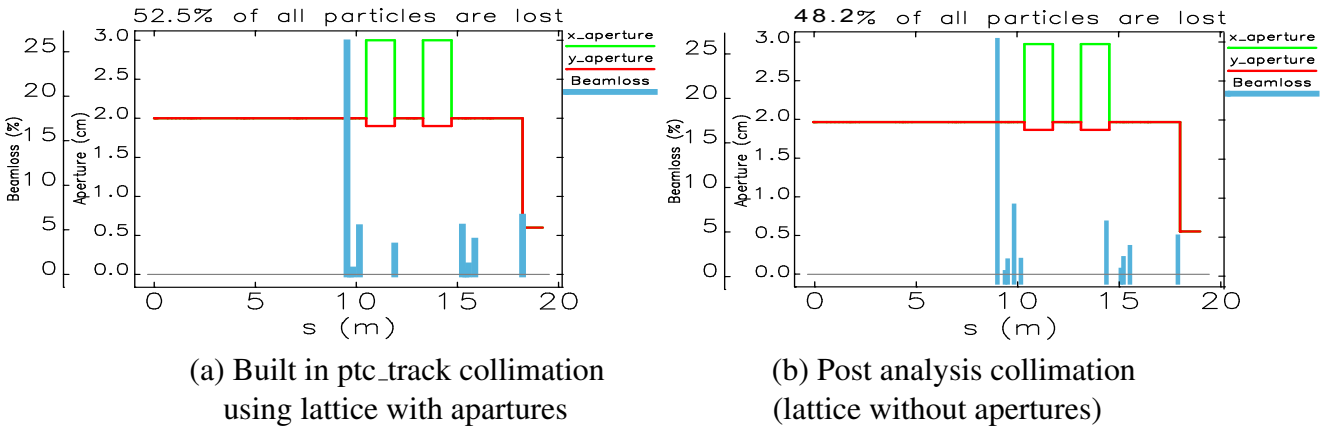


Figure 40: *Beam loss distribution along the line for an ideal trajectory* (one seed) and $4*\epsilon_{x/y}$ beam at 0.3 MeV/u.

calculated, for designed requirements, namely, for the most rigid beam at 10 MeV/u ($B\rho = 2.054$ Tm) and $A/q=4.5$ at the reference (measurement) radius $R = 20$ mm [13]. In Tables of App. 7.7.4 column 3 (relative value $b_n^{rel.}$) is obtained from column 2 (absolute value $b_n^{abs.}$) by normalizing on the main field components b_1 . Note that no skew components were considered for an ideal case of design magnets, which are supposed to be perfectly symmetric [13]. It is also assumed that an ideal magnet should be independent on the beam rigidity $B\rho$, however in reality a possible dependence may exist, for example, due to saturations [13].

7.7.1 Integrated multipoles in MADX convension

Complex notation of harmonics components [13] reads

$$B_y + iB_x = \sum_{n=1}^{\infty} (b_n + ia_n) \left(\frac{x + iy}{R} \right)^{n-1}, \quad (9)$$

where R is a reference radius. Eq. (9) contains *intrinsic magnet length* L , so that field B is defined in [Tm].

With MADX notation the multipoles are written as

$$B_y + iB_x = B\rho \sum_{m=0}^{\infty} (k_m + ij_m) \frac{(x + iy)^m}{m!}, \quad (10)$$

where $K_{ml} = k_m \cdot L$ and $J_{ml} = j_m \cdot L$ are integrated multipolar kicks in [m^{-m}]. Note that the MADX multipole notation includes already the beam rigidity $B\rho$ related to the particle energy.

The conversion of integrated field harmonic (App. 7.7.4) into integrated multipolar kicks in MADX is obtained via ratio of Eqs. (9) and (10) [14]

$$K_{nl} = \frac{n!}{B\rho \cdot R^n} \cdot b_{n+1}^{abs.} = \frac{n!}{\alpha^* \cdot R^n} \cdot b_{n+1}^{rel.}, \quad (11)$$

where $\alpha^* = B\rho / \int b_1 dl$.

7.7.2 Sextupolar and octupolar components in dipoles

Dominating in 45° dipoles harmonics $n = 3, 4$ in App. 7.7.4 were recalculated via Eq. (11) and considered in the MADX simulation [13]. The corresponding multipoles were specified as absolute errors using DKN option in EFCOMP subroutine

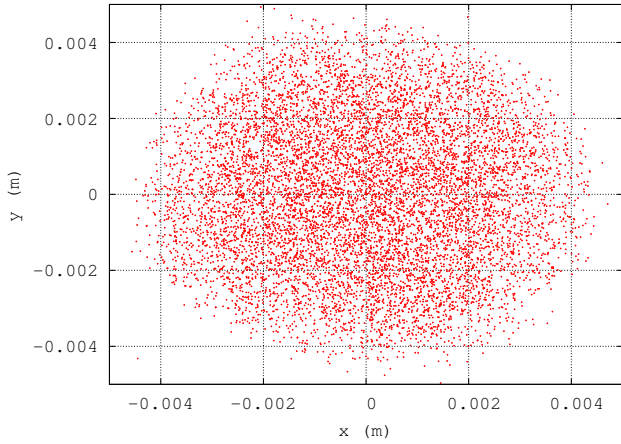
```
md.error := 1.0e-3*(2*ranf()-1.0);
md.error2 := - 1.0*(2*ranf()-1.0); !sextupole  $K_{2l} = - 1.0$  [ $\text{m}^{-2}$ ]
md.error3 := - 30.0*(2*ranf()-1.0); !octupole  $K_{3l} = - 30.0$  [ $\text{m}^{-3}$ ]
EFCOMP, ORDER :=0, RADIUS := 0.02, DKN := {0,0,md.error2,md.error3},
DKNR := {md.error};
```

Phase-space plots at the exit of the achromat for linear case of *all static errors* and including the *doubled* K_{2l} and K_{3l} are presented in Fig. 41 (a) and (b), respectively. No visible effect is found for the reason that the impact of nonlinear components is negligible compare with an effect of natural chromaticity (uncompensated).

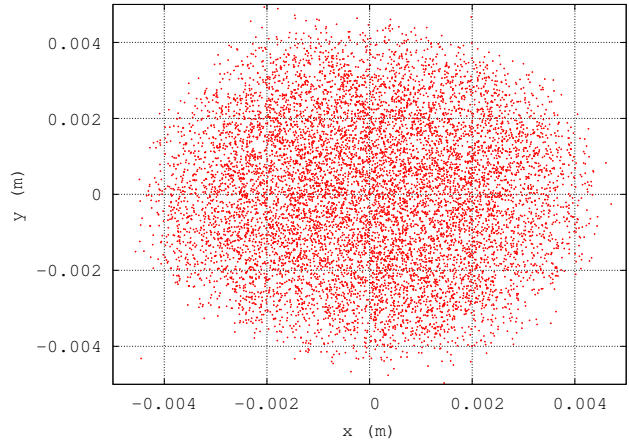
7.7.3 Steerers misalignment and sextupolar components. Multipoles in quadrupoles

Combined effect of sextupolar components in steerers and their missalignments produces a quadrupolar feed-down, which may introduce a β -beating. Steerers were missaligned by 1000 μm and the sextupolar harmonic from App. 7.7.4 using Eq. (11) were introduced

```
select, flag = error, clear;
select, flag = error, class = "steerer";
md.error2s := + 0.2*(2*ranf()-1.0); !sextupole  $K_{2l} = + 0.2$  [ $\text{m}^{-2}$ ]
EFCOMP, ORDER:=0, RADIUS:= 0.02, DKN:={0,0,md.error2s};
```

(a) Linear case of *all static errors*



(b) $K_{2l} = -2.0 \text{ [m}^{-2}\text{]}, K_{3l} = -60.0 \text{ [m}^{-3}\text{]}$

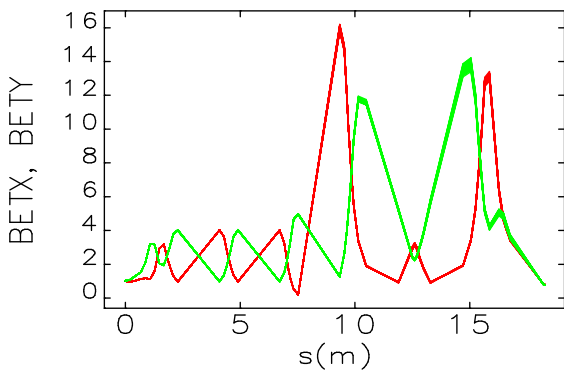
Figure 41: Phase-space plots at the exit of the achromat.

```
EALIGN, dx := 1.0e-3*tgauss(2.4), dy := 1.0e-3*tgauss(2.4);
select, flag = error, class = "steerer";
```

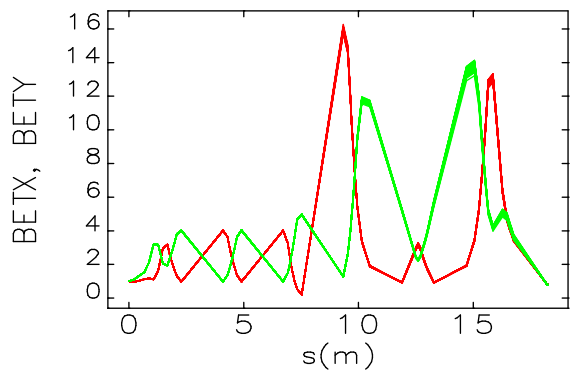
Also dodecapole and 20-pole multipoles $n = 6, 10$ were estimated from App. 7.7.4 via Eq. (11) for quadrupole magnets and were introduced in the simulation

```
q1.error := 1.0e-3*(2*ranf()-1.0);
q5.error := -3.1*1.0e+5*(2*ranf()-1.0); !dodecapole  $K_{5l} = -3.1 \cdot 10^5 \text{ [m}^{-5}\text{]}$ 
q9.error := -1.97*1.0e+15*(2*ranf()-1.0); !20-pole  $K_{9l} = -1.97 \cdot 10^{15} \text{ [m}^{-9}\text{]}$ 
EFCOMP, ORDER := 1, RADIUS := 0.02, DKN := {0,0,0,0,0,q5.error,0,0,0,q9.error},
DKNR := {0,q1.error};
```

Comparison of β -functions for the case of all linear static errors and with the nonlinear components in dipoles, quadrupoles and steerers with $1000 \mu\text{m}$ misalignment is presented in Fig. 42. No visible effect was obtained.



(a) Linear case of *all static errors*



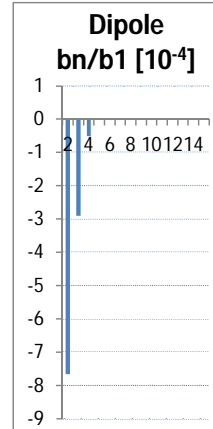
(b) Including nonlinear harmonics

Figure 42: β -functions for *all static errors* linear case (a) and with nonlinear harmonics and steerer misalignment (b).

7.7.4 Harmonic components for HIE-ISOLDE new magnets

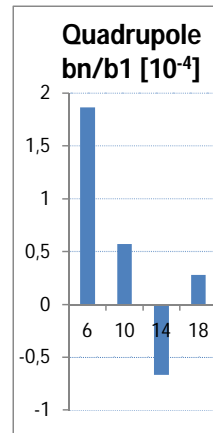
45 deg dipole harmonics

Harmonic number n	Integrated field harmonics @ R = 20 mm bn [Tm]	Integrated field normalized harmonics bn/b1 [10 ⁻⁴]	Multipole order MADX
1	1,6140989	10000	0
2	-1,24E-03	-7,66374377	1
3	-4,68E-04	-2,89860264	2
4	-8,08E-05	-0,50070804	3
5	9,37E-07	5,80E-03	4
6	-3,44E-06	-0,02134037	5
7	3,55E-06	0,02197266	6
8	1,60E-06	9,90E-03	7
9	1,43E-06	8,83E-03	8
10	-1,46E-06	-9,04E-03	9
11	-1,63E-06	-0,01009942	10
12	1,37E-06	8,47E-03	11
13	1,97E-06	0,01218207	12
14	-7,70E-07	-4,77E-03	13
15	-2,09E-06	-0,01297073	14



Quadrupole harmonics

Harmonic number n	Integrated field harmonics @ R = 20 mm bn [Tm]	Integrated field normalized harmonics bn/b1 [10 ⁻⁴]	Multipole order MADX
2	-1,00E-01	10000	1
6	-1,87E-05	1,8661324	5
10	-5,75E-06	5,75E-01	9
14	6,64E-06	-6,63E-01	13
18	-2,81E-06	0,28132223	17



Steerer harmonics

Harmonic number n	Integrated field harmonics @ R = 20 mm bn [Tmm]	Integrated field normalized harmonics bn/b1 [10 ⁻⁴]	Multipole order MADX
1	9,1096205	10000	0
3	0,080698	88,5854667	2
5	2,23E-03	2,44659804	4
7	-6,33E-04	-0,69508677	6
9	2,78E-05	0,03047627	8

